

Inferring potential landslide damming using slope stability, geomorphic constraints and run-out analysis; case study from the NW Himalaya

Vipin Kumar^{1*}, Imlirenla Jamir², Vikram Gupta³, Rajinder K. Bhasin⁴

¹Georisks and Environment, Department of Geology, University of Liege, Liege, Belgium

²Public Works Department (PWD), Nagaland, India

³Wadia Institute of Himalayan Geology, Dehradun, India

⁴Norwegian Geotechnical Institute, Oslo, Norway

*Correspondence: v.chauhan777@gmail.com; B-18, B-4000, Sart-Tilman, Liege, Belgium

1 ABSTRACT

2 Prediction of potential landslide damming has been a difficult process owing to the
3 uncertainties related to the landslide volume, resultant dam volume, entrainment, valley
4 configuration, river discharge, material composition, friction, and turbulence associated with
5 material. In this study, instability pattern of landslides, geomorphic indices, post failure run-
6 out predictions, and spatio-temporal pattern of rainfall and earthquake are explored to predict
7 the potential landslide damming sites. The Satluj valley, NW Himalaya is chosen as a case
8 study area. The study area has witnessed landslide damming in the past and incurred \$ ~30M
9 loss and 350 lives in the last four decades due to such processes. Forty-four active landslides
10 that cover a total $\sim 4.81 \pm 0.05 \times 10^6 \text{ m}^2$ area and $\sim 34.1 \pm 9.2 \times 10^6 \text{ m}^3$ volume are evaluated to
11 identify those landslides that may result in the potential landslide damming. Out of forty-four,
12 five landslides covering a total volume of $\sim 26.3 \pm 6.7 \times 10^6 \text{ m}^3$ are noted to form the potential
13 landslide dams. Spatio-temporal varying pattern of the rainfall in the recent years enhanced
14 the possibility of landslide triggering and hence of the potential damming. These five
15 landslides also revealed $24.8 \pm 2.7\text{m}$ to $39.8 \pm 4.0\text{m}$ high debris flow in the run-out
16 predictions.

17 **Key words:** Landslide damming, Slope stability; Run-out; Himalaya

1.0 INTRODUCTION

Landslide damming is a normal geomorphic process in the narrow river valleys and has been one of the most disastrous natural processes (Dai et al. 2005; Gupta and Sah 2008; Delaney and Evans 2015; Fan et al. 2020). There have been many studies that explored the damming characteristics (Li et al. 1986; Costa and Schuster 1988; Takahashi and Nakawaga 1993; Ermini and Casagli 2003; Fujisawa et al. 2009; Stefanelli et al. 2016; Kumar et al. 2019a). However, studies concerning the prediction of potential landslide dams and their stability at regional scale have been relatively rare, particularly in Himalaya despite a history of landslide damming and flash floods (Gupta and Sah 2008; Ruiz-Villanueva et al. 2016; Kumar et al. 2019a). In order to identify the landslides that have potential to form dams, following factors have been main requisites; (i) pre- and post-failure behaviour of landslide slopes (ii) landslide volume, stream power, and morphological setting of the valley (Kumar et al. 2019a).

To understand the pre-failure pattern, the Finite Element Method (FEM) based slope stability evaluation has been among the most widely used approaches for the complex slope geometry (Griffiths and Lane 1999; Jing 2003; Jamir et al. 2017; Kumar et al. 2018). However, the selection of input parameters in the FEM analysis and set of assumptions (material model, failure criteria, and convergence) may also result in the uncertainty in the final output (Wong 1984; Cho 2007; Li et al. 2016). Input parameters based uncertainty can be resolved by performing the parametric analysis, whereas the utilization of most appropriate criteria can minimize the uncertainty caused by assumptions. Post-failure behavior of landslides can be understood using the run-out analysis (Hungr et al. 1984; Hutter et al. 1994; Rickenmann and Scheidl 2013). These methods could be classified into empirical/statistical and dynamical categories (Rickenmann 2005). Owing to the flexibility in rheology, solution approach, reference frame, and entrainment, dynamic models have been relatively more realistic for the site-specific problems (Corominas and Mavrouli 2011). Though the different numerical models have different advantages and limitations, Voellmy rheology (friction and turbulence) (Voellmy 1955; Salm 1993) based Rapid Mass Movement ~~Software~~-Simulation (RAMMS) (Christen et al. 2010) model has been used widely owing to the inclusion of rheological and entrainment rate flexibility.

Apart from the pre and post-failure pattern, landslide volume, stream power and morphological setting of the valley are crucial to infer the potential landslide damming.

50 Morphological Obstruction Index (MOI) and Hydro-morphological Dam Stability Index
51 (HDSI) have been widely used geomorphic indices to infer the potential of landslide dam
52 formation and their temporal stability (Costa and Schuster 1988; Ermini and Casagli 2003;
53 Stefanelli et al. 2016).

54 The NW Himalaya has been one of most affected terrains by the landslides owing to the
55 active tectonics and multiple precipitation sources i.e., Indian Summer Monsoon (ISM) and
56 Western Disturbance (Dimri et al. 2015). The NW Himalaya has also accommodated ~51 %
57 of all the landslides in India during yrs. 1800-2011 (Parkash 2011). The Satluj River valley,
58 NW Himalaya is one such region that has claimed ~350 lives and loss of minimum 30 million
59 USD due to the landslides and associated floods in the last four decades and holds a high
60 potential for landslide damming and resultant floods (Ruiz-Villanueva et al. 2016; Kumar et
61 al. 2019a). Therefore, Satluj valley is taken as a case study area, of which 44 active landslides
62 belonging to the different litho-tectonic regimes are modeled using the FEM
63 technique. Multiple slope sections and a range of values of different input parameters are
64 used to perform the parametric study. In order to determine the human population that might
65 be affected by these landslides, census statistics are also used. The MOI and HDSI are used to
66 determine the potential of landslide dam formation and their stability, respectively. In view of
67 the role of rainfall and earthquake as main landslide triggering factors, spatio-temporal
68 regime of these two factors is also discussed. Run-out prediction of certain landslides is also
69 performed to understand the role of run-out in the potential landslide damming. This study
70 provides a detailed insight into the regional instability pattern, associated uncertainty, and
71 potential landslide damming sites and hence it can be replicated in other hilly terrain
72 witnessing frequent landslides and damming.

73 2.0 STUDY AREA

74 The study area is located between the Moorang (31°36'1" N, 78°26' 47" E) and Rampur town
75 (31°27'10" N, 77°38' 20" E) in the Satluj River valley, NW Himalaya (Fig. 1). The Satluj
76 River flows across the Tethyan Sequence (TS), Higher Himalaya Crystalline (HHC), Lesser
77 Himalaya Crystalline (LHC), and Lesser Himalaya Sequence (LHS). The TS in the study area
78 comprises slate/phyllite and schist and has been intruded by the biotite-rich granite i.e.,
79 Kinnaur-Kailash Granite (KKG) near the Sangla Detachment (SD) fault (Sharma 1977;
80 Vannay et al. 2004). The SD fault separates the TS from the underlying crystalline rockmass
81 of the HHC. Migmatitic gneiss marks the upper part of the HHC, whereas the base is marked

82 by the kyanite-sillimanite gneiss rockmass (Sharma 1977; Vannay et al. 2004; Kumar et al.
83 2019b). The Main Central Thrust (MCT) fault separates the HHC from the underlying
84 schist/gneissic rockmass of the LHC. The LHC comprises mica schist, carbonaceous schist,
85 quartzite, and amphibolite. A thick zone of gneiss i.e., Wangtu Gneissic Complex (WGC) is
86 exposed in the LHC, which comprises augen gneiss and porphyritic granitoids. The LHC is
87 delimited at the base by the Munsiri Thrust (MT) fault that is thrust over the Lesser
88 Himalaya Sequence (LHS) rockmass. The MT contains breccia, cataclastic, and fault gouge
89 (Sharma 1977; Vannay et al. 2004; Kumar et al. 2019b). The LHS in the study area consists
90 of quartz-arenite (Rampur Quartzite) with bands of phyllite, meta-volcanics, and paragneiss
91 (Sharma 1977).

92 The present study covers forty-four active landslides (20 debris slides, 13 rock falls, and 11
93 rock avalanches) along the study area (Table 1) that have been mapped recently by Kumar et
94 al. (2019b). Field photographs of some of these landslides are presented in Fig. 2. The TS and
95 LHS in the study area have been subjected to the tectonic tranquility with exhumation rates as
96 low as 0.5 - 1.0 mm/yr, whereas the HHC and LHC region comprise 1.0 - 4.5 mm/yr rate of
97 exhumation (Thiede et al. 2009). The MCT fault region and the WGC are noted to have
98 maximum exhumation rate (i.e., ~4.5 mm/yr) that is evident from the deep gorges in these
99 regions (Fig. 2c, 2e). Further, a majority of the earthquake events in the study area in the last
100 7 decades have been related to the N-S oriented Kaurik - Chango Fault (KCF) (Kundu et al.
101 2014; Hazarika et al. 2017; International Seismological Centre Catalogue 2019). The climate
102 zones in the study area shows a spatial variation from the humid (~800 mm/yr) in the LHS to
103 the semi-arid (~200 mm/yr) in the TS (Kumar et al. 2019b). The HHC acts as a transition
104 zone where climate varies from semi-humid to semi-arid in the SW-NE direction. This
105 transition has been attributed to the 'orographic barrier' nature of the HHC that marks the
106 region in its north as 'orographic interior' and the region to its south as the 'orographic front'
107 (Wulf et al. 2012; Kumar et al. 2019b).

108 The landslides in the study area have been a consistent threat to the socio-economic condition
109 of the nearby human population (Gupta and Sah 2008; Ruiz-Villanueva et al. 2016; Kumar et
110 al. 2019a). Therefore, the human population in the vicinity of each landslide was also
111 determined by considering the villages/town in that region. It is to note that total 25,822
112 people reside in the 500 m extent of the 44 landslide slopes and about 70 % of this population
113 is residing in the reach of debris slide type landslides. Since the Govt. of India follows a 10
114 year gap in census statistics, the human population data was based on last official i.e.,

115 Census-2011. The next official census is due in year 2021. The population density in the
116 Indian Himalayan region was estimated to be 181/km² in the year 2011 that might grow to
117 212/km² in 2021 with a decadal growth rate of 17.3% (<https://censusindia.gov.in>, retrieved on
118 02 Sep 2020; <http://gbpihedenviis.nic.in>, retrieved on 02 Sep 2020).

119 3.0 METHODOLOGY

120 ~~In order to determine the potential landslide damming sites along the Satluj River valley, NW~~
121 ~~Himalaya, The~~ methodology involved the field data collection, satellite imagery analysis,
122 laboratory analyses, ~~Finite Element Method (FEM) bases~~ slope stability ~~evaluation~~ modelling,
123 ~~parametric analysis, application of Morphological Obstruction Index (MOI) & Hydro-~~
124 ~~morphological Dam Stability Index (HDSI) and debris run out analysis~~ geomorphic indices,
125 ~~rainfall/earthquake pattern~~ and run-out modelling. Details are as follows;

126 3.1 Field data, satellite imagery processing, and laboratory analyses

127 The field work involved rock/soil sample collection from each landslide location, rockmass
128 joint mapping, and N-type Schmidt Hammer Rebound (SHR) measurement. The joints were
129 included in the slope models for the FEM based slope stability analysis. Dataset involving the
130 joint details is available in the data repository (Kumar et al. 2020). The SHR values were
131 obtained as per International Society of Rock Mechanics (ISRM) standard (Aydin 2008). The
132 Cartosat-1 satellite imagery and field assessment were used to finalize the location of slope
133 sections (2D) of the landslides. The Cartosat-1 imagery has been used widely for the
134 landslide related studies (Martha et al. 2010). The Cartosat-1 Digital Elevation Model
135 (DEM), prepared using the Cartosat-1 stereo imagery, was used to extract the slope sections
136 of the landslides using the Arc GIS-10.2 software. Details of the satellite imagery are
137 mentioned in Table 2.

138 The rock/soil samples were analyzed in the National Geotechnical Facility (NGF) and Wadia
139 Institute of Himalayan Geology (WIHG) laboratory, India. The rock samples were drilled and
140 smoothed for Unconfined Compressive Strength (UCS) (IS: 9143-1979) and ultrasonic test
141 (CATS Ultrasonic (1.95) of Geotechnical Consulting & Testing Systems. The Ultrasonic test
142 was conducted to determine the density, elastic modulus, and Poisson's ratio of rock samples.
143 The soil samples were tested for grain size analysis (IS: 2720-Part 4-1985), UCS test (IS:
144 2720-Part 10-1991), and direct shear test (IS: 2720-Part 13- 1986). If the soil samples
145 contained < 5% fines (< 75 mm), hydrometer test was not performed for the remaining fine

146 material. In the direct shear test, soil samples were sheared under the constant normal stress
147 of 50, 100 and 150 kN/m². The UCS test of soil was performed under three different rates of
148 movements i.e., 1.25 mm/min, 1.50 mm/min and 2.5 mm/min.

149 3. 2 Slope stability modelling

150 The Finite Element Method (FEM) was used along with the Shear Strength Reduction (SSR)
151 technique to infer the critical Strength Reduction Factor (SRF), Shear Strain (SS), and Total
152 Displacement (TD) in the 44 landslide slopes using the RS2 software. The SRF has been
153 observed to be similar in nature as the Factor of Safety (FS) of the slope (Zienkiewicz et al.
154 1975; Griffiths and Lane 1999). To define the failure in the SSR approach, non-convergence
155 criteria was used (Nian et al. 2011). The boundary condition with the restraining movement
156 was applied to the base and back, whereas the front face was kept free for the movement (Fig.
157 3). In-situ field stress was adjusted in view of dominant stress i.e., extension or compression
158 by changing the value of the coefficient of earth pressure (k). The $k = \sigma_h/\sigma_v = 0.5$ was used in
159 extensional regime, whereas $k = \sigma_h/\sigma_v = 1.5$ was used in compressional regime. The Tethyan
160 Sequence has been observed to possess the NW-SE directed extensional regime. The
161 structures in the upper part of the HHC are influenced by the east directed extension along the
162 SD fault. The lower part, however, comprises the signs of the SW directed compression along
163 the Main Central Thrust. In contrast to the HHC, structures in the Lesser Himalaya
164 Crystalline and Munsiri Thrust region are influenced by the compressional regime. In the
165 Lesser Himalaya Sequence region, the SW directed compressional regime has been observed
166 on the basis of the SW verging folds, crenulation cleavage, and other features (Vannay et al.
167 2004).

168 The soil and rock mass were used in the models through the Mohr-Coulomb (M-C) failure
169 criterion (Coulomb 1776; Mohr 1914) and Generalized Hoek-Brown (GHB) criterion (Hoek
170 et al. 1995), respectively. The parallel- statistical distribution of the joints with normal-
171 distribution joint spacing in the rock mass was applied through the Barton-Bandis (B-B) slip
172 criterion (Barton and Choubey 1977; Barton and Bandis 1990). Plane strain triangular
173 elements having 6 nodes were used through the graded mesh in the models. Details of the
174 criteria used in the FEM analysis are mentioned in Table 3. Dataset involving the value of
175 input parameters used in the FEM analysis is available in the data repository (Kumar et al.
176 2020). It is to note that the FEM analysis is performed under the static load i.e., field stress
177 and body force. The dynamic analysis is not performed, at present, in absence of any major

178 seismic events in the region in the last 4 decades (sec. 4.3) and lack of reliable dynamic load
179 data of nearby major seismic events.

180 To understand the uncertainty caused by the selection of 2D slope section, multiple slope
181 sections were taken, wherever possible. More than one slope sections were modeled for each
182 debris slide, whereas for the rock falls/ rock avalanche only one slope section was chosen due
183 to the limited width of the rock falls/rock avalanche in the study area. To find out the relative
184 influence of different input parameters on the final output, a parametric study was performed.
185 In the parametric study for debris slides, Akpa landslide (S.N.5 in Fig. 3), Pangi landslide
186 (S.N.13 in Fig. 3), and Barauni Gad landslide (S.N.38 in Fig. 3) were chosen, whereas Tirung
187 khad (S.N.2 in Fig.3) and Chagaon landslide (S.N.21 in Fig. 3) were considered to represent
188 rock fall. Baren Dogri (S.N.7 in Fig. 3) landslide was used to represent the rock avalanches.
189 The selection of these landslides for the parametric study was based on the following two
190 factors; (1) to choose the landslides from different litho-tectonic regime, (2) representation of
191 varying stress regime i.e., extensional, compressional, and relatively stagnant. The Parametric
192 study of the debris slide models involved following 9 parameters; field stress coefficient,
193 stiffness ratio, cohesion and angle of friction of soil, elastic modulus and Poisson's ratio of
194 soil, rockmass modulus, Poisson's ratio and uniaxial compressive strength of rock. For the
195 rockfalls/rock avalanche, following 6 parameters; uniaxial compressive strength of rock,
196 rockmass modulus of rock, Poisson's ratio of rock, 'mi' parameter, stiffness ratio, and field
197 stress coefficient were used. The 'mi' is a Generalized Hoek-Brown (GHB) parameter that is
198 equivalent to the angle of friction of Mohr-coulomb (M-C) criteria.

199 3.3 Geomorphic indices

200 Considering the possibility of landslide dam formation in case of slope failure, following
201 geomorphic indices are also used;

202 (i) Morphological Obstruction Index (MOI)

203
$$MOI = \log (V_l/W_v)$$
 Eq. 1

204 (ii) Hydro-morphological Dam Stability Index (HDSI)

205
$$HDSI = \log (V_d/A_b.S)$$
 Eq. 2

206 Where, V_d (dam volume) = V_l (landslide volume), m^3 ; A_b is upstream catchment area (km^2);
207 W_v is width of ~~dammed-the~~ valley (m) and S is local slope gradient of river channel (m/m).
208 Though the resultant dam volume could be higher or lower than the landslide volume owing
209 to the slope entrainment, rockmass fragmentation, retaining of material at the slope, and
210 washout by the river (Hung and Evans 2004; Dong et al. 2011), dam volume is assumed to
211 be equal to landslide volume for the worst case. By utilizing the comprehensive dataset of
212 ~300 landslide dams of Italy, Stefanelli et al. (2016) have classified the MOI into (i) non-
213 formation domain: $MOI < 3.00$ (ii) uncertain evolution domain: $3.00 < MOI < 4.60$ and (iii)
214 formation domain: $MOI > 4.60$. By utilizing the same dataset, Stefanelli et al. (2016) defined
215 the HDSI into following categories (i) instability domain: $HDSI < 5.74$ (ii) uncertain
216 determination domain: $5.74 < HDSI < 7.44$ and (iii) Stability domain: $HDSI > 7.44$.

217 3. 4 Rainfall and Earthquake regime

218 Precipitation in the study area owes its existence to the Indian Summer Monsoon (ISM) and
219 Western Disturbance (WD) and varies spatially-temporally due to various local and regional
220 factors (Gadgil et al. 2007; Hunt et al. 2018). Therefore, we have taken the TRMM_3B42
221 daily rainfall data of years 2000-2019 at four different locations; Moorang, Kalpa, Nachar,
222 and Rampur (Locations mentioned in Fig. 1). The dataset of earthquake events ($2 < M < 8$) in
223 and around study area during the years 1940-2019 was retrieved from the ISC catalogue
224 (<http://www.isc.ac.uk/iscbulletin/search/catalogue/>, retrieved on 02 March 2020) to determine
225 the spatio-temporal pattern.

226 3. 5 Run-out modelling

227 Since the study area has witnessed many disastrous landslides, mostly rainfall triggered, and
228 flash floods in past (Gupta and Sah 2008; Ruiz-Villanueva et al. 2016), run-out analysis was
229 performed to understand the post-failure scenario. Such run-out predictions will also be
230 helpful to ascertain the possibility of damming because various studies have noted the river
231 damming by the debris flows (Li et al. 2011; Braun et al. 2018; Fan et al. 2020). Therefore,
232 the landslides that have potential to form the dams based on the indices (sec. 3.3) are
233 evaluated for such run-out analysis.

234 In this study, Voellmy rheology (Voellmy 1955; Salm 1993) based Rapid Mass Movement
235 Simulation (RAMMS) (Christen et al. 2010) model is used to understand the run-out pattern.
236 The RAMMS for debris flow uses the Voellmy friction law and divides the frictional

resistance into a dry-Coulomb type friction (μ) and viscous-turbulent friction (ξ). The frictional resistance S (Pa) is thus;

$$S = \mu N + (\rho g u^2) / \xi \quad \text{Eq. 3}$$

where N ; $\rho g h \cos(\phi)$ is the normal stress on the running surface, ρ ; density, g ; gravitational acceleration, ϕ ; slope angle, h ; flow height and $u = (u_x, u_y)$, consisting of the flow velocity in the x- and y-directions. In this study, a range of friction (μ) and turbulence (ξ) values, apart from other input parameters, are used to eliminate the uncertainty in output (Table 4). Generally, the values for μ and ξ parameters are achieved using the reconstruction of real events through the simulation and subsequent comparison between the dimensional characteristics of real and simulated event. However, the landslides in the study area merge with the river floor and/or are in close proximity and hence there is no failed material left from the previous events to reconstruct. Therefore, the μ and ξ values were taken in a range in view of topography of landslide slope and run-out path, landslide material, similar landslide events/material, and based on previous studies/models (Hurlimann et al. 2008; Rickenmann and Scheidl 2013; RAMMS v.1.7.0). Since these landslides are relatively deep in nature and we are of understanding that during the slope failure, irrespective of type of trigger, entire loose material might not slide down, the depth of landslide is taken as only $1/4$ (thickness) in the run-out calculation. Further, a release area concept (for unchanneled flow or block release) was used for the run-out simulation. During the field visits, no specific flow channels (or gullies) were found on the landslide slopes except a few centimeters deep seasonal flow channels for S. N. 5 and S.N. 15 landslides (Table 1). However, the data pertaining to the spatial-temporal information of discharge at these two landslides was not available. Therefore, the release area concept was chosen because it has been more appropriate when the flow path (e.g. gully) and its possible discharge on the slope is uncertain (RAMMS v.1.7.0).

4.0 RESULTS

4.1 Slope instability regime and parametric output

Results indicated that out of 44 landslides, 31 are in meta-stable state ($1 \leq FS \leq 2$) and 13 in unstable state ($FS < 1$) (Fig. 4). Most of the unstable landslides are debris slides, whereas the majority of the meta-stable landslides are rock fall/rock avalanche. Debris slides constitute ~ 90 % and ~99 % of the total area and volume, respectively of the unstable landslides. It is to

note that about ~70 % of the total human population along the study area resides in the vicinity (~500 m) of these unstable debris slides (Fig. 4). Rock falls/Rock avalanches constitute ~84 % and ~78 % of the area and volume, respectively of the meta-stable landslides. Out of total 20 debris slides, 12 debris slides are found to be in unstable stage, whereas 8 in the meta-stable condition (Fig. 4). These 20 debris slides occupy $\sim 1.9 \pm 0.02 \times 10^6 \text{ m}^2$ area and $\sim 26 \pm 6 \times 10^6 \text{ m}^3$ volume. While comparing the Factor of Safety (FS) with the Total Displacement (TD) and Shear Strain (SS), nonlinear poor correlation is achieved (Fig. 5). Since, the TD and SS present a relatively good correlation (Fig. 5), only the TD is used further along with the FS. The TD ranges from $7.4 \pm 8.9 \text{ cm}$ to $95.5 \pm 10 \text{ cm}$ for the unstable debris slides and $\sim 18.8 \text{ cm}$ for meta-stable landslides (Fig. 4). Out of 13 rockfalls, 1 belongs to the unstable state and 12 to the meta-stable state (Fig. 4). The TD varies from 0.4 to 80 cm with the maximum for Bara Kamba rockfall (S.N. 31). Out of 11 rock avalanches, 1 belongs to the unstable state and 10 to the meta-stable state (Fig. 4). The TD varies from 6.0 to 132.0 cm with the maximum for the Kandar rock avalanche (S.N. 25). Relatively higher TD is obtained by the rock fall and rock avalanche of the Lesser Himalaya Crystalline region (Fig. 4). The landslides of the Higher Himalaya Crystalline (HHC), Kinnaur Kailash Granite (KKG) and Tethyan Sequence (TS), despite being only 17 out of the total 44 landslides, constituted ~ 67 % and ~ 82 % of the total area and total volume of the landslides.

The Factor of Safety (FS) of debris slides is found to be relatively less sensitive to the change in the value of input parameters than the Total Displacement (TD) (Fig. 6). In case of Akpa (Fig. 6a) and Pangi landslide (Fig. 6b), soil friction and field stress have more influence on the FS. However, for the TD, field stress, elastic modulus and Poisson's ratio of the soil are relatively more controlling parameters. The FS and TD of the Barauni Gad landslide (Fig. 6c) are relatively more sensitive to soil cohesion and 'mi' parameter. Therefore, it can be inferred that the FS of debris slides is more sensitive to soil friction and field stress, whereas TD is mostly controlled by the field stress and deformation parameters i.e, elastic modulus and Poisson's ratio. Similar to the debris slides, the FS of rock falls and rock avalanche are found to be relatively less sensitive than TD to the change in the value of input parameters (Fig. 7). Tirung Khad rock fall (Fig. 7a) and Baren Dogri rock avalanche (Fig. 7b) show dominance of 'mi' parameter and field stress in the FS as well as in TD. In case of Chagaon rock fall (Fig. 7c), Poisson's ratio and UCS have relatively more influence on FS and TD. Thus, it can be inferred that the rock fall/rock avalanche are more sensitive to 'mi' parameter and field stress.

300 4.2 Potential landslide damming

301 Based on the MOI, out of total 44 landslides, 5 (S.N. 5, 7, 14, 15, 19) are observed to be in
302 the formation domain, 15 in uncertain domain, and 24 in non-formation domain (Fig. 8a).
303 These five landslides that have potential to dam the river in case of slope failure
304 accommodate $\sim 26.3 \pm 6.7 \times 10^6 \text{ m}^3$ volume (Fig. 9 a-e). In terms of temporal stability (or
305 durability), out of these five landslides, only one landslide (S.N. 5) is noted to attain the
306 'uncertain' domain, whereas the remaining four show 'instability' (Fig. 8b,d). The lacustrine
307 deposit in the upstream of Akpa landslide (S.N. 5) in Fig. 9a implies the signs of landslide
308 damming in the past also (Fig. 10). The 'uncertain' temporal stability indicates that the
309 landslide dam may be stable or unstable depending upon the stream power and landslide
310 volume, which in turn are dynamic factors and may change owing to the changing climate
311 and/or tectonic event. The landslides that have been observed to form the landslide dam but
312 are noted to be in temporally unstable category (S.N. 7, 14, 15, 19) are still considerable
313 owing to the associated risks of lake-impoundment and generation of secondary landslides.
314 Urni landslide (S.N. 19) (Fig. 9e) that damaged the part of National Highway road (NH)-05
315 has already partially dammed the river since year 2016 and holds potential for the further
316 damming (Kumar et al. 2019a). Apart from the S.N. 5 and S.N. 19 landslides, remaining
317 landslides (S.N. 7, 14, 15) belong to the Higher Himalaya Crystalline (HHC) region that has
318 been observed to accommodate many landslide damming and subsequent flash floods events
319 in the geological past (Sharma et al. 2017).

320 4.3 Rainfall and Earthquake regime

321 In order to explain the spatio-temporal variation in the rainfall, topographic profile of the
322 study area is also plotted along with the rainfall variation (Fig. 11a). The temporal
323 distribution of rainfall is presented at annual, monsoonal i.e., Indian Summer Monsoon
324 (ISM): June-September and non-monsoonal i.e., Western Disturbance (WD): Oct-May (Fig.
325 11b-d) level. Rainfall data of the years 2000-2019 revealed a relative increase in the annual
326 rainfall since the year 2010 (Fig. 11b). The Kalpa region (orographic barrier) received a
327 relatively more annual rainfall than the Rampur, Nachar and Moorang region throughout the
328 time period, except the year 2017. The rainfall dominance at Kalpa is more visible in non-
329 monsoonal season (Fig. 11d). It may be due to its orographic influence on the saturated winds
330 of the WD (Dimri et al. 2015). Further, the rainfall during the monsoon season that was

331 dominant at the Rampur region till year 2012 gained dominance at Kalpa region since the
332 year 2013 (Fig. 11c).

333 Extreme rainfall events of June 2013 that resulted in the widespread slope failure in the NW
334 Himalaya also caused landslide damming at places (National Disaster Management
335 Authority, Govt. of India, 2013; Kumar et al. 2019a). Similar to the year 2013, the year 2007,
336 2010 and 2019 also witnessed enhanced annual rainfall and associated flash floods and/or
337 landslides in the region (hpenviis.nic.in, retrieved on March 1, 2020; sandrp.in, retrieved on
338 March 1, 2020). However, the contribution of the ISM and WD associated rainfall has been
339 variable in these years (Fig. 11). Such frequent but inconsistent rainfall events that possess
340 varied (temporally) dominance of the ISM and WD are noted to owe their occurrence to the
341 following local and regional factors; El-Nino Southern Oscillation (ENSO), Equatorial Indian
342 Ocean Circulation (EIOC), and planetary warming (Gadgil et al. 2007; Hunt et al. 2018). The
343 orographic setting is noted to act as a main local factor as evident from the relatively more
344 rainfall (total precipitation=1748±594 mm/yr.) at Kalpa region (orographic barrier) in the
345 non-monsoon and monsoon season from the year 2010 onwards (Fig. 11). Prediction of the
346 potential landslide damming sites in the region revealed that four (S.N. 7, 14, 15, 19) out of
347 five landslides that can form the dam belong to this orographic barrier region. Therefore, in
348 view of the prevailing rainfall trend since the year 2010, regional factors, discussed above,
349 and orographic setting, precipitation triggered slope failure events cannot be denied in the
350 future. Such slope failure events, if occurred, at the predicted landslide damming sites may
351 certainly dam the river.

352 The seismic pattern revealed that the region has been hit by 1662 events during the years
353 1940-2019 with the epicenters located in and around the study area (Fig. 12a). However,
354 ~99.5 % of these earthquake events had a magnitude of less than 6.0 and only 8 events are
355 recorded in the range of 6.0 to 6.8 M_s (International Seismological Centre 2019). Out of these
356 8 events, only one event i.e., 6.8 M_s (19th Jan. 1975) has been noted to induce the widespread
357 slope failures in the study area (Khattari et al. 1978). The majority of the earthquake events in
358 the study area has occurred in the vicinity of the N-S oriented trans-tensional Kaurik -
359 Chango Fault (KCF) that accommodated the epicenter of 19th Jan. 1975 earthquake (Hazarika
360 et al. 2017; <http://www.isc.ac.uk/iscbulletin/search/catalogue/>, retrieved on 02 March 2020).
361 About 95% of the total 1662 events had their focal depth within 40 km (Fig. 12b). Such a
362 relatively low magnitude - shallow seismicity in the region has been related to the Main

Himalayan Thrust (MHT) decollement as a response to the relatively low convergence ($\sim 14 \pm 2$ mm/yr) of India and Eurasia plates in the region (Bilham 2019) (Fig. 12c). Further, the arc (Himalaya)-perpendicular Delhi-Haridwar ridge that is under thrusting the Eurasian plate in this region has been observed to be responsible for the spatially varied *low* seismicity in the region (Hazarika et al. 2017). Thus, though the study area has been subjected to frequent earthquakes, chances of earthquake-triggered landslides have been relatively low in comparison to rainfall-triggered landslides and associated landslide damming. For this reason and the lack of reliable dynamic load of major earthquake event, we have performed the *static* modelling in the present study. However, we intend to perform the *dynamic* modelling in near future if the reliable dynamic load data will be available.

4.4 Run-out analysis

All five landslides (S.N. 5, 7, 14, 15, 19 in Fig. 9) that are observed to form potential landslide dam in case of slope failure were also used for the run-out analysis. Results are as follows;

4.4.1 Akpa landslide (S.N. 5)

Though it is difficult to ascertain that how much part of the debris flow might contribute in the river blockage, it will certainly block the river in view of ~ 38 m high debris material with ~ 50 m wide run-out across the channel in this narrow part of river valley (Fig. 9a) even at maximum value of coefficient of friction (i.e., $\mu = 0.3$) (Fig. 13a). It is to note that not only the run-out extent but flow height also decreases on increasing the friction value (Fig. 13a.1-13a.3). The maximum friction can take into account the shear resistance by slope material and the bed-load on the river channel. However, apart from the frictional characteristics of run-out path, turbulence of debris flow also controls its dimension and hence consequences like potential damming. Therefore, different values of turbulence coefficient (ξ) were used (Table 4). The resultant flow height (representing 9 sets of debris flow obtained using $\mu = 0.05, 0.1$ and 0.3 and $\xi = 100, 200$ and 300 m/s²) attains its peak value i.e., 39.8 ± 4.0 m at the base of central part of landslide (Fig. 14a).

4.4.2 Baren dogri landslide (S.N. 7)

At the maximum friction value ($\mu = 0.4$), Baren dogri landslide is noted to attain a peak value of flow height i.e., ~ 30 m at the base of central part of landslide (Fig. 13b). Similar to the valley configuration around the Akpa landslide (sec 4.4.1), river valley attains a narrow/deep

gorge setting here also (Fig. 9b). The maximum value of debris flow height obtained using the different μ and ξ values is 25.6 ± 2.1 m (Fig. 14b). Flow material is also noted to attain more run-out in upstream direction of river (~1100 m) than in the downstream direction (~800 m). This spatial variability in the run-out length might exist due to the river channel configuration as river channel in upstream direction is relatively narrower than the downstream direction.

4.4.3 Pawari landslide (S.N. 14)

Pawari landslide attains maximum flow height of ~20 m at the maximum friction of run-out path ($\mu=0.4$) (Fig. 13c). The resultant debris flow that is achieved using the different values of μ and ξ parameters attains a peak value of 24.8 ± 2.7 m and decreases gradually with a run-out of ~1500 m in upstream and downstream direction (Fig. 14c). This landslide resulted in the relatively long run-out of ~1500 in the upstream and downstream direction. Apart from the landslide volume that affects the run-out extent, valley morphology also controls it as evident from the previous landslides. The river channel in upstream and downstream direction from the landslide location is observed to be narrow (Fig. 9c).

4.4.4 Telangi landslide (S.N. 15)

Telangi landslide is noted to result in peak debris flow height of ~24 m at the maximum friction ($\mu=0.4$) (Fig. 13d). It is to note that on increasing the friction of run-out path, flow run-out decreased along the river channel but increased across the river channel resulting into possible damming. The debris flow after taking into account different values of μ and ξ parameters attains a peak value of 25.0 ± 4.0 m (Fig. 14d). Similar to Baren dogri landslide (S.N. 7), material attained more run-out in upstream direction of river (~1800 m) than in downstream direction (~600 m) that attributes to narrower river channel in upstream than the downstream direction. The downstream side attains wider river channel due to the traversing of Main Central Thrust (MCT) fault in the proximity (Fig. 1). Since Pawari and Telangi landslide (S.N 14 & 15) are situated ~500 m from each other, their respective flow run-outs might mix in the river channel resulting into disastrous cumulative effect.

4.4.5 Urni landslide (S.N. 19)

Urni landslide attained a peak value of ~44 m of debris flow height at the maximum friction value ($\mu=0.4$) (Fig. 13e). After taking into account different values of μ and ξ parameters, the debris flow attained a height of 26.3 ± 1.8 m (Fig. 14e). Relatively wider river channel in

425 downstream direction (Fig. 9e) is considered to results in long run-out in downstream
426 direction than in the upstream.

427 5.0 DISCUSSION

428 Present study aimed to determine the potential landslide damming sites in the Satluj River
429 valley, NW Himalaya. In order to achieve this objective, 44 landslides were considered. At
430 first, slope stability evaluation of all the slopes was performed alongwith the parametric
431 evaluation. Then the geomorphic indices i.e., Morphological Obstruction Index (MOI) and
432 Hydro-morphological Dam Stability Index (HDSI) were used to predict the formation of
433 potential landslide dam and their subsequent stability. Rainfall and earthquake regime were
434 also explored in the study area. Finally, run-out analysis was performed of those landslides
435 that have been observed to form the potential landslide dam.

436 The MOI revealed that out of 44 landslides, five (S.N. 5, 7, 14, 15, 19) have potential to form
437 the landslide dam (Fig. 8, 9). On evaluating the stability of such potential dam sites using the
438 HDSI, the landslide (S.N. 5) is noted to attain an 'uncertain' domain ($5.74 < \text{HDSI} < 7.44$) in
439 terms of dam stability. The uncertain term implies that the resultant dam may be stable or
440 unstable depending upon the landslide/dam volume, upstream catchment area (or water
441 discharge) and slope gradient (sec 3.3). Since this landslide (S.N.5) presents clear signs of
442 having already formed a dam in the past, as indicated by the alternating fine-coarse layered
443 sediment deposit (or lake deposit) in the upstream region (Fig. 10), recurrence can't be
444 denied. Further, run-out analysis of landslide has predicted $39.8 \pm 4.0\text{m}$ high debris flow in
445 the event of failure that will block the river completely (Fig. 13a, 14a). However, the
446 durability of the blocking can't be ascertained as it is subjected to the volume of landslide
447 that will be retained at the channel and river discharge.

448 Remaining four landslides (S.N. 7, 14, 15, 19), though showed instability i.e., $\text{HDSI} < 5.74$ at
449 present, may form the dam in near future as the region accommodating these landslides has
450 been affected by such damming and subsequent flash floods in the past (Sharma et al. 2017).
451 The last one of these i.e., S.N. 19 (Urni landslide) has already dammed the river partially and
452 holds potential to completely block the river in near future (Kumar et al. 2019a). Run-out
453 analysis of these landslides (S.N. 7, 14, 15, 19) has predicted $25.6 \pm 2.1\text{m}$, $24.8 \pm 2.7\text{m}$, $25.0 \pm$
454 4.0m and $26.3 \pm 1.8\text{m}$ flow height, respectively that will result in temporary blocking of the
455 river (Fig. 13,14). These findings of run-out indicate towards the blocking of river in the

456 event of slope failure, irrespective of durability, despite the conservative depth as input
457 because only $\frac{1}{4}$ of landslide thickness is used in the run-out analysis (sec. 3.5).

458 Stability evaluation of these five landslide slopes (S.N. 5, 7, 14, 15, 19) that have potential to
459 form landslide dam revealed that except one landslide (S.N.7) that is meta-stable, remaining
460 four belong to the unstable category (Fig. 4). Further, except this landslide that is meta-stable
461 (S.N. 7), remaining four unstable landslide slopes are debris slide in nature. It is noteworthy
462 to discuss the implications of $FS < 1$. The Factor of Safety (FS) in the Shear Strength
463 Reduction (SSR) approach is a factor by which the existing shear strength of material is
464 divided to determine the critical shear strength at which failure occurs (Zienkiewicz et al.
465 1975; Duncan 1996). Since the landslide represents a failed slope i.e., critical shear strength $>$
466 existing shear strength, $FS < 1$ is justifiable. Further, the failure state of a slope in the FEM can
467 be defined by different criteria; the FS of same slope may vary a little depending upon the
468 usage of failure criteria and the convergence threshold (Abramson et al. 1996; Griffiths and
469 Lane 1999).

470 The possible causes of instability ($FS < 1$) may be steep slope gradient, ~~weak~~
471 ~~lithology~~~~rockmass having low strength~~, and joints. Three (S.N. 7, 14, 15) out of these five
472 landslides that have potential to form the dam belong to the tectonically active Higher
473 Himalaya Crystalline (HHC). The notion of steep slope gradient cannot be generalized
474 because the HHC accommodates most voluminous ($\sim 10^5$ - 10^7 m³) landslides (Fig. 4). These
475 deep seated landslides must require smooth slope gradient to accommodate the voluminous
476 overburden. Further, the HHC comprises ~~strong lithology~~ i.e., gneiss having high
477 compressive strength and Geological Strength Index (Supplementary Table 2, Kumar et al.
478 2020)~~therefore~~, therefore the notion of ~~weak lithology~~~~low strength rockmass~~ also may not be
479 appropriate. However, the jointed rock mass that owes its origin to numerous small scale
480 folds, shearing, and faults associated with the active orogeny process can be considered as the
481 main factor for relatively more instability of debris slide type landslides. Since, the study area
482 is subjected to the varied stress regime caused by the tectonic structures (Vannay et al. 2004)
483 thermal variations (Singh et al. 2015), and anthropogenic cause (Lata et al. 2015), joints may
484 continue to develop and destabilize the slopes. Apart from this inherent factor like joints,
485 external factors like rainfall and exhumation rate may also contribute to instability of these
486 landslides. This region receives relatively more annual rainfall owing to orographic barrier

487 setting (Fig. 11) and is subjected to relatively high exhumation rate of 2.0-4.5 mm/yr (Thiede
488 et al. 2009).

489 Two landslides (S.N. 5, 19) that are also capable to form potential landslide dam (Fig. 8, 9a;
490 e) and are also unstable ($FS < 1$) in nature (Fig. 4) do not belong to the HHC. The first
491 landslide (S.N. 5) exists at the lithological contact of schist of the Tethyan Sequence and
492 Kinnaur Kailash Granite rockmass. A regional normal fault i.e., Sangla Detachment (SD)
493 passes through this contact. Few studies suggest that the SD is an outcome of reactivation of
494 former thrust fault that has resulted in intense rockmass shearing (Vannay et al. 2004; Kumar
495 et al. 2019b). Owing to its location in the orographic interior region, hillslopes receives very
496 low annual rainfall (Fig. 11) and thus comprises least vegetation on the hillslopes. The lack of
497 vegetation on hillslopes has been observed to result in low shear strength of material and
498 hence in the instability (Kokutse et al. 2016). Thus, lithological contrast, rockmass shearing,
499 and lack of vegetation are the main reasons of instability of S.N. 5 landslide. The second
500 landslide (S.N. 19) belongs to the inter-layered schist/gneiss rockmass of the Lesser
501 Himalaya Crystalline (LHC) and is situated at the orographic front where rainfall increases
502 suddenly (Fig. 11). Further, this region is also subjected to the high exhumation rate of 2.0-
503 4.5 mm/yr (Thiede et al. 2009). Therefore, lithological contrast, high rainfall and high
504 exhumation rate are considered as the main reasons of instability of this landslide slope.

505 The landslides that could not result into the river damming are mostly in the LHC and Lesser
506 Himalaya Sequence (LHS) region. These regions consist of a majority of the rock fall and
507 rock avalanches that are generally of meta-stable category (Fig. 4). Despite the narrow valley
508 setting, landslides in these regions may not form the potential landslide dam, at present,
509 owing to the relatively less landslide volume. The possible causes of this meta-stability may
510 be high compressive strength and geological strength index of gneiss (Kumar et al. 2020),
511 dense vegetation on the hillslopes (Chawla et al. 2012), relatively less sheared rock mass in
512 comparison to the HHC region, and relatively less decrease in land use/landcover (Lata et al.
513 2015). Maximum Total Displacement (TD) is also associated with the rock fall and rock
514 avalanche of this region (Fig. 4).

515 In the parametric study, soil friction and in-situ stress are noted to affect the FS most in case
516 of the debris slide, whereas the FS of rock fall and rock avalanche are mainly controlled by
517 the 'mi' and the in-situ stress. The 'mi' is a GHB criteria parameter that is equivalent to the
518 friction in the M-C criteria. For the TD of the debris slides, field stress, elastic modulus and

Poisson's ratio, whereas for rock falls and rock avalanches, 'mi' parameter and in-situ stress played the dominant role (Fig. 6,7). The friction has been a controlling factor for the shear strength and its decrease has been observed to result in the shear failure of slope material (Matsui and San 1992). Since the rainfall constitutes an important role in decreasing the friction of slope material by changing the pore water pressure regime (Rahardjo et al. 2005), frequent extreme rainfall events in the study area since the year 2013 (Kumar et al. 2019a) amplifies the risk of hillslope instability. Furthermore, the in-situ field stress that has been compressional and/or extensional owing to the orogenic setting in the region may also enhance the hillslope instability (Eberhardt et al. 2004; Vannay et al. 2004). Deformation parameters e.g. elastic modulus and Poisson's ratio are also observed to affect the displacement in slope models of the debris slides. Similar studies in other regions have also noted the sensitivity of the elastic modulus and Poisson's ratio on the slope stability (Zhang and Chen 2006).

The study area has been subjected to extreme rainfalls since the year 2010 and received widespread slope failures and flash-floods (Fig. 11b). Three (S.N. 7,14,15 in Fig. 9) out of five potential landslide dams belong to the Higher Himalaya Crystalline (HHC) that receives relatively more rainfall (Fig. 11). Contrary to the along 'Himalayan' arc distribution of earthquakes, the study area has received most of the earthquakes around the N-S oriented Kaurik-Chango Fault (Fig. 12a). However, the only major earthquake event has been M_w 6.8 earthquake on 19th Jan. 1975 that resulted in the widespread landslides (Khattri et al. 1978). The low-magnitude seismicity in the region has been attributed to the northward extension of the Delhi-Haridwar ridge (Hazarika et al. 2019), whereas the shallow nature is subjected to the MHT ramp structure in the region that allows strain accumulation at shallow depth (Bilham 2019). Thus, earthquake has not been a major landslide triggering process in the region. Finally, the word "active landslide" refers to the hillslope that is still subjected to the slope failures caused by the various factors. The word "landslide" can be perceived in the following three ways; pre-failure deformations, failure itself, and post-failure displacement (Terzaghi 1950; Cruden & Varnes, 1996; Hungr et al., 2014). Landslide slopes in this study pertains to the post-failure state that are categorized into "unstable" and "meta-stable" stages based on their existing FS. Furthermore, if an active landslide is not categorized as "unstable", it means that the existing slope geometry provides it a "meta-stable" stage that might transform into an unstable stage with time due to the stability controlling parameters (Sec. 4.1). A supplementary table involving all the details like landslides dimension, factor of

[safety, and geomorphic indices output of each landslide is provided in the data repository \(Kumar et al. 2020\).](#)

In view of the possible uncertainties in the predictive nature of study, following assumptions and then resolutions were made;

- To account the effect the spatial variability in the slope geometry, 3D models have been in use for the last decade (Griffiths and Marquez 2007). However, the pre-requisite for the 3D models involves the detailed understanding of slope geometry and material variability in the subsurface that was not possible in the study area considering steep and inaccessible slopes. Therefore, multiple 2D sections were chosen, wherever possible. To account the effect of sampling bias and material variability, a range of values of input parameters was used (sec. 4.1).
- Determination of the debris thickness has been a major problem in the landslide volume measurement particularly in the steep, narrow river valleys of the NW Himalaya. Therefore, the thickness was approximated by considering the relative altitude of the ground on either side of the deposit, as also performed by Innes (1983). It was assumed that the ground beneath the deposit is regular.
- The resultant dam volume could be different from the landslide volume due to the entrainment, rockmass fragmentation, pore water pressure, size of debris particles, and washout of landslide material by the river (Hung and Evans 2004; Dong et al. 2011; Yu et al. 2014). Therefore, dam volume is presumed to be equal to landslide volume for the worst-case scenario (sec. 3.3). Stream power is manifested by the upstream catchment area and local slope gradient in the geomorphic indices. It may also vary at temporal scale owing to the temporally varying water influx from glaciers and precipitation systems i.e., ISM and WD (Gadgil et al. 2007; Hunt et al. 2018). Though our study is confined to the spatial scale at present, the findings remain subjected to the change at temporal scale.
- The RAMMS model (Voellmy 1955; Salm 1993; Christen et al. 2010) requires the calibrated friction and turbulence values for the run-out analysis. Though the previous debris flow events don't have trace in the study area owing to the convergence of landslide toe with the river channel, a range of μ and ξ values were used in the study in view of the material type and run-out path characteristics.

Despite these uncertainties, such studies are required to minimize the risk and avert the possible disasters in the terrain where human population is bound to live in the proximity of unstable landslides.

CONCLUSION

Out of forty-four landslides that are studied, five landslides are noted to form the potential landslide dam, if failure occurs. Though the blocking duration is difficult to predict, upstream and downstream consequences of these damming events can't be overlooked as the region has witnessed many damming and flash floods in the past. These five landslides comprise a total landslide volume of $26.3 \pm 6.7 \text{ M m}^3$. The slopes of four landslides (debris slides) out of these five are unstable, whereas the remaining one (rock avalanche) is meta-stable. Field observations and previous studies have noted the damming events by these landslides (or the region consisting these landslides) in the past also. Since the area is witnessing enhanced rainfall and flash floods since year 2010, findings of the run-out analysis that revealed $24.8 \pm 2.7\text{m}$ to $39.8 \pm 4.0\text{m}$ high material flow from these landslides become more crucial. The parametric analysis for the slope stability evaluation revealed that the angle of internal friction of soil or ' m_i ' (equivalent to the angle of internal friction) of the rockmass, and *in-situ* field stress are the most controlling parameters for the stability of slopes.

ACKNOWLEDGEMENT

VK and IJ acknowledge the constructive discussion on the regional scale study with Prof. H.B. Havenith, Prof. D.V. Griffiths, and Prof. D.P. Kanungo. VG and RKB acknowledge the financial help through the project MOES/Indo-Nor/PS-2/2015. Authors are thankful to the RAMMS developer for the license. Authors are also thankful to Prof. Xuanmei Fan (Associate Editor) and two anonymous reviewers for their insightful comments that improved the final manuscript.

Conflict of Interest

The authors declare that they have no conflict of interest.

Dataset Availability

The dataset is uploaded in the open access repository (*Mendeley data*) as Kumar et al. (2020).

Author contribution

612 VK conceived the idea and collected the field data. VK and IJ performed the laboratory
 613 analysis. All authors contributed to the dataset compilation, numerical simulation and
 614 geomorphic interpretations. All authors contributed to the writing of the final draft.

615 REFERENCES

- 616 Abramson, L. W., Lee, T. S., Sharma, S. 1996. "Slope stability and stabilization methods".
 617 New York. Wiley.
- 618 Aydin, A. 2008. "ISRM suggested method for determination of the Schmidt hammer rebound
 619 hardness: revised version". In: R. Ulusay (ed) *The ISRM Suggested Methods for Rock
 620 Characterization, Testing and Monitoring: 2007–2014*. Springer, Cham, pp. 25-33.
- 621 Barton, N. and Bandis, S. 1982. "Effects of block size on the shear behavior of jointed rock".
 622 In: *Proc. 23rd US symposium on rock mechanics*. American Rock Mechanics
 623 Association, 739-760.
- 624 Barton, N. and Choubey, V. 1977. "The shear strength of rock joints in theory and practice".
 625 *Rock mechanics* 10(1-2):1-54.
- 626 Barton, N. R. 1972. "A model study of rock-joint deformation. International journal of rock
 627 mechanics and mining sciences". *Geomech. Abstr.* 9 (5): 579-602.
- 628 Barton, N. R. and Bandis, S. C. 1990. "Review of predictive capabilities pf JRC-JCS model in
 629 engineering practice". In: Barton N and Stephansson O (ed) *Rock Joints*, Rotterdam,
 630 pp. 603-610.
- 631 Bhasin, R. and Kaynia, A. M. 2004. "Static and dynamic simulation of a 700-m high rock
 632 slope in western Norway". *Engineering Geology* 71(3-4): 213-226.
- 633 Bilham, R. 2019. "Himalayan earthquakes: a review of historical seismicity and early 21st
 634 century slip potential". *Geological Society, London, Special Publications*. 483(1):423-
 635 82.
- 636 Bowles, J. E. 1996. *Foundation Analysis and Design*, 5th ed., McGraw-Hill, New York, pp.
 637 750.
- 638 Braun, A., Cuomo, S., Petrosino, S., Wang, X. and Zhang, L., 2018. "Numerical SPH
 639 analysis of debris flow run-out and related river damming scenarios for a local case
 640 study in SW China". *Landslides* 15 (3), 535-550.
- 641 Cai, M., Kaiser, P. K., Tasaka, Y. and Minami, M. 2007. "Determination of residual strength
 642 parameters of jointed rock masses using the GSI system". *International Journal of Rock
 643 Mechanics and Mining Sciences* 44(2): 247-265.
- 644 Chawla, A., Kumar, A., Lal, B., Singh, R.D. and Thukral, A.K. 2012. "Ecological
 645 Characterization of High Altitude Himalayan Landscapes in the Upper Satluj River
 646 Watershed, Kinnaur, Himachal Pradesh, India". *Journal of the Indian Society of Remote
 647 Sensing* 40(3): 519-539.
- 648 Cho, S. E. 2007. "Effects of spatial variability of soil properties on slope stability".
 649 *Engineering Geology* 92(3-4): 97-109.
- 650 Christen, M., Kowalski, J., Bartelt, P. 2010. "RAMMS: Numerical simulation of dense snow
 651 avalanches in three-dimensional terrain". *Cold Regions Science and Technology*. 63: 1-
 652 14.

Corominas, J. and Mavrouli, J., 2011. "Living with landslide risk in Europe: Assessment, effects of global change, and risk management strategies". *Documento tecnico, safeland. 7th Framework Programme Cooperation Theme*, 6.

Costa, J. E. and Schuster, R. L. 1988. "The formation and failure of natural dams". *Geological society of America bulletin* 100(7): 1054-1068.

Coulomb, C. A. 1776. "An attempt to apply the rules of maxima and minima to several problems of stability related to architecture". *Mémoires de l'Académie Royale des Sciences* 7: 343-382.

[Cruden, D. M. and Varnes, D. J. 1996. Landslides: investigation and mitigation. In: Landslide types and processes. Transportation Research Board, US National Academy of Sciences, Special Report, \(247\).](#)

Dai, F.C., Lee, C.F., Deng, J.H. and Tham, L.G. 2005. "The 1786 earthquake-triggered landslide dam and subsequent dam-break flood on the Dadu River, southwestern China". *Geomorphology* 65(3): 205-221.

Deere, D. U. and Miller, R. P. 1966. "Engineering classification and index properties for intact rock". Illinois University at Urbana, USA.

Delaney, K. B. and Evans, S. G. 2015. "The 2000 Yigong landslide (Tibetan Plateau), rockslide-dammed lake and outburst flood: review, remote sensing analysis, and process modelling". *Geomorphology* 246, 377-393.

Dimri, A.P., Niyogi, D., Barros, A.P., Ridley, J., Mohanty, U.C., Yasunari, T. and Sikka, D.R. 2015. "Western disturbances: A review". *Reviews of Geophysics* 53(2): 225-246

Dong, J.J., Tung, Y.H., Chen, C.C., Liao, J.J. and Pan, Y.W. 2011. "Logistic regression model for predicting the failure probability of a landslide dam". *Engineering Geology* 117(1): 52-61.

Duncan, J. M. 1996. "State of art: limit equilibrium and finite element analysis of slopes". *Journal of Geotechnical Engineering Division, ASCE* 122 (7): 577-596.

Eberhardt, E., Stead, D. and Coggan, J. S. 2004. "Numerical analysis of initiation and progressive failure in natural rock slopes—the 1991 Randa rockslide". *International Journal of Rock Mechanics and Mining Sciences* 41(1): 69-87.

Ermini, L. and Casagli, N. 2003. "Prediction of the behaviour of landslide dams using a geomorphological dimensionless index". *Earth Surface Processes and Landforms* 28(1): 31-47.

Fan, X, Dufresne, A, Subramanian, SS, Strom, A, Hermanns, R, Stefanelli, CT, Hewitt, K, Yunus, AP, Dunning, S, Capra, L and Geertsema, M. 2020. "The formation and impact of landslide dams—State of the art". *Earth-Science Reviews*, 203:103116.

Fujisawa, K., Kobayashi, A. and Aoyama, S. 2009. "Theoretical description of embankment erosion owing to overflow". *Geotechnique* 59(8): 661-671.

Gadgil, S., Rajeevan, M. and Francis, P.A. 2007. "Monsoon variability: Links to major oscillations over the equatorial Pacific and Indian oceans". *Current Science*. 93(2):182-94.

Griffiths, D. V. and Lane, P. A. 1999. "Slope stability analysis by finite elements". *Geotechnique* 49(3): 387-403.

Griffiths, D. V. and Marquez, R. M. 2007. "Three-dimensional slope stability analysis by elasto-plastic finite elements". *Geotechnique* 57(6): 537-546.

697 Gupta, V. and Sah, M. P. 2008. "Impact of the trans-Himalayan landslide lake outburst flood
698 (LLOF) in the Satluj catchment, Himachal Pradesh, India". *Natural Hazards* 45(3):
699 379-390.

700 Gupta, V., Nautiyal, H., Kumar, V., Jamir, I., and Tandon, R. S. 2016. "Landslides hazards
701 around Uttarkashi Township, Garhwal Himalaya, after the tragic flash flood in June
702 2013". *Natural Hazards* 80: 1689-1707

703 [Hung, O., Leroueil, S., and Picarelli, L. 2014. "The Varnes classification of landslide types,
704 an update". *Landslides* 11 \(2\): 167-194.](#)

705 Hürlimann, M., Rickenmann, D., Medina, V. and Bateman, A. 2008. "Evaluation of
706 approaches to calculate debris-flow parameters for hazard assessment". *Eng Geol*
707 102:152-163

708 Havenith, H.B., Torgoev, I. and Ischuk, A. 2018. "Integrated Geophysical-Geological 3D
709 Model of the Right-Bank Slope Downstream from the Rogun Dam Construction Site,
710 Tajikistan". *International Journal of Geophysics* 1-17.

711 Hazarika, D., Wadhawan, M., Paul, A., Kumar, N. and Borah, K. 2017. "Geometry of the
712 Main Himalayan Thrust and Moho beneath Satluj valley, northwest Himalaya:
713 Constraints from receiver function analysis". *Journal of Geophysical Research: Solid*
714 *Earth*. 122(4):2929-45.

715 Hoek, E. and Brown, E.T. 1997. "Practical estimates of rock mass strength". *International*
716 *Journal of Rock Mechanics and Mining Science* 34(8):1165-1186

717 Hoek, E. and Diederichs, M.S. 2006. "Empirical estimation of rock mass modulus".
718 *International Journal of Rock Mechanics and Mining Sciences* 43 (2): 203-15.

719 Hoek, E., Kaiser, P.K. and Bawden, W.F. 1995. *Support of Underground Excavations in Hard*
720 *Rock*. Rotterdam: A. A. Balkema.

721 Hung, O. and Evans, S.G. 2004. "Entrainment of debris in rock avalanches: an analysis of a
722 long run-out mechanism". *Geological Society of America Bulletin* 116(9-10): 1240-
723 1252.

724 Hung, O., Morgan, G.C. and Kellerhals, R. 1984. "Quantitative analysis of debris torrent
725 hazards for design of remedial measures". *Can Geotech J* 21:663-677

726 Hunt, K.M., Turner, A.G. and Shaffrey, L.C. 2018. "The evolution, seasonality and impacts of
727 western disturbances". *Quarterly Journal of the Royal Meteorological Society*.
728 144(710):278-90.

729 Hutter, K., Svendsen, B. and Rickenmann, D. 1994. "Debris flow modelling: a review".
730 *Continuum mechanics and thermodynamics* 8: 1-35.

731 Innes, J. L. 1983. "Debris flows". *Progress in Physical Geography* 7(4): 469-501.

732 IS: 2720 (Part 10)-1991. "Method of test for soils: Determination of unconfined compressive
733 strength". In: *Bureau of Indian Standards, Delhi, India*.

734 IS: 2720 (Part 13)-1986. "Method of test for soils: Direct shear test". In: *Bureau of Indian*
735 *Standards, New Delhi, India*.

736 IS: 2720 (Part 4)-1985. "Methods of test for soils: Grain size analysis". In: *Bureau of Indian*
737 *Standards, New Delhi, India*.

738 IS: 9143-1979. "Method for the determination of unconfined compressive strength of rock
739 materials". In: *Bureau of Indian Standards, New Delhi, India*.

Formatted: Font: Italic

740 Jamir, I., Gupta, V., Kumar, V. and Thong, G.T. 2017. "Evaluation of potential surface
741 instability using finite element method in Kharsali Village, Yamuna Valley, Northwest
742 Himalaya". *Journal of Mountain Science* 14(8): 1666-1676.

743 Jamir, I., Gupta, V., Thong, G.T. and Kumar, V. 2019. "Litho-tectonic and precipitation
744 implications on landslides, Yamuna valley, NW Himalaya". *Physical Geography* 41(4)
745 365-388.

746 Jang, H.S., Kang, S.S. and Jang, B.A. 2014. "Determination of joint roughness coefficients
747 using roughness parameters". *Rock mechanics and rock engineering* 47(6): 2061-73.

748 Jing, L. 2003. "A review of techniques, advance and outstanding issues in numerical
749 modelling for rock mechanics and rock engineering". *International Journal of Rock*
750 *Mechanics and Mineral Science* 40:283-353.

751 Khattri, K., Rai, K., Jain, A.K., Sinvhal, H., Gaur, V.K. and Mithal, R.S. 1978. "The Kinnaur
752 earthquake, Himachal Pradesh, India, of 19 January, 1975". *Tectonophysics*. 49(1-2):1-
753 21.

754 Kokutse, N.K., Temgoua, A.G.T. and Kavazović, Z. 2016. "Slope stability and vegetation:
755 Conceptual and numerical investigation of mechanical effects". *Ecological Engineering*
756 86: 146–153.

757 Kumar, V., Gupta, V. and Jamir, I. 2018. "Hazard Evaluation of Progressive Pawari Landslide
758 Zone, Kinnaur, Satluj Valley, Higher Himalaya, India". *Natural Hazards* 93: 1029-
759 1047.

760 Kumar, V., Gupta, V., Jamir, I. and Chatteraj, S.L. 2019a. "Evaluation of potential landslide
761 damming: Case study of Urni landslide, Kinnaur, Satluj valley, India". *Geosci. Front.*
762 10(2): 753-767.

763 Kumar, V., Gupta, V. and Sundriyal, Y.P. 2019b. "Spatial interrelationship of landslides,
764 litho-tectonics, and climate regime, Satluj valley, Northwest Himalaya". *Geol. J.* 54:
765 537–551.

766 Kumar, V., Jamir, I., Gupta, V. and Bhasin, R.K. 2020. "Dataset used to infer regional slope
767 stability, NW Himalaya". *Mendeley Data*. DOI: 10.17632/jh8b2rh8nz.1

768 Kundu, B., Yadav, R.K., Bali, B.S., Chowdhury, S. and Gahalaut, V.K. 2014. "Oblique
769 convergence and slip partitioning in the NW Himalaya: Implications from GPS
770 measurements." *Tectonics* 33: 2013-2024.

771 Lata, R., Rishi, S., Talwar, D. and Dolma, K. 2015. "Comparative Study of Landuse Pattern in
772 the Hilly Area of Kinnaur District, Himachal Pradesh, India". *International Journal of*
773 *Innovative Science, Engineering & Technology* 2(4): 559-565.

774 Li, D.Q., Qi, X.H., Cao, Z.J., Tang, X.S., Phoon, K.K. and Zhou, C.B. 2016. "Evaluating
775 slope stability uncertainty using coupled Markov chain". *Computers and*
776 *Geotechnics* 73:72-82.

777 Li, T., Schuster, R.L. and Wu, J. 1986. "Landslide dams in south-central China". In: *Proc.*
778 *Landslide dams: processes, risk, and mitigation*, ASCE Convention, Washington, 146-
779 162.

780 Li, M.H., Sung, R.T., Dong, J.J., Lee, C.T., and Chen, C.C. 2011. "The formation and
781 breaching of a short-lived landslide dam at Hsiaolin village, Taiwan-Part II: Simulation
782 of debris flow with landslide dam breach". *Engineering Geology* 123: 60-71.

Martha, T.R., Kerle, N., Jetten, V., van Westen, C.J. and Kumar, K.V. 2010. "Landslide volumetric analysis using Cartosat-1-derived DEMs". *IEEE Geoscience and remote sensing letters* 7(3): 582-586.

Matsui, T. and San, K.C. 1992. "Finite element slope stability analysis by shear strength reduction technique". *Soils and foundations* 32(1): 59-70.

Mohr, O. 1914. "Abhandlungen aus dem Gebiete der Technischen Mechanik" (2nd ed). Ernst, Berlin.

NDMA: National Disaster Management Authority. 2013. Annual report, Government of India, Delhi.

Nian, T.K., Chen, G.Q., Wan, S.S. and Luan, M.T. 2011. "Non-convergence Criterion on Slope Stability FE Analysis by Strength Reduction Method". *Journal of Convergence Information Technology* 6:78-88.

O'Brien, J.S., Julien, P.Y. and Fullerton, W.T. 1993. "Two-dimensional water flood and mud flood simulation". *J Hydraul Eng* 119:244-260.

Parkash, S. 2011. "Historical records of socio-economically significant landslides in India". *J South Asia Disaster Studies* 4(2): 177-204.

Rahardjo, H., Lee, T.T., Leong, E.C. and Rezaur, R.B. 2005. "Response of a residual soil slope to rainfall". *Canadian Geotechnical Journal* 42(2): 340-351.

Rickenmann, D. 2005. "Runout prediction methods". In: Jakob M, Hungr O (eds) *Debris-flow hazards and related phenomena*. Praxis/Springer, Berlin/Heidelberg, pp. 305-324.

Rickenmann, D., and Scheidl, C. 2013. "Debris-Flow Runout and Deposition on the Fan". *M. Schneuwly-Bollschweiler et al. (eds.), Dating Torrential Processes on Fans and Cones, Advances in Global Change Research* 47, DOI 10.1007/978-94-007-4336-6 5

Ruiz-Villanueva, V., Allen, S., Arora, M., Goel, N. K. and Stoffel, M. 2016. "Recent catastrophic landslide lake outburst floods in the Himalayan mountain range". *Progress in Physical Geography* 41 (1): 3-28.

Salm, B., 1993. "Flow, flow transition and runout distances of flowing avalanches". *Ann. Glaciol.* 18: 221-226.

Sharma, S., Shukla, A.D., Bartarya, S.K., Marh, B.S. and Juyal, N. 2017. "The Holocene floods and their affinity to climatic variability in the western Himalaya, India". *Geomorphology* 290: 317-334.

Sharma, K. K. 1977. "A contribution to the geology of Satluj Valley, Kinnaur, Himachal Pradesh, India". *Colloques Internationaux du CNRS* 268: 369-378.

Singh, D., Gupta, R.D. and Jain, S.K. 2015. "Statistical analysis of long term spatial and temporal trends of temperature parameters over Sutlej river basin, India". *J. Earth Syst. Sci.* 124 (1): 17-35.

Stefanelli, C.T., Segoni, S., Casagli, N. and Catani, F. 2016. "Geomorphic indexing of landslide dams evolution". *Engineering Geology* 208: 1-10.

Takahashi, T. And Nakagawa, H. 1993. "Flood and debris flow hydrograph due to collapse of a natural dam by overtopping". In: *Proc. Hydraulic Engineering, Japan*, 37: 699-704.

Terzaghi, K. 1950. "Mechanism of Landslides". In: *Application of Geology to Engineering Practice. Geol. Soc. Am* 83-123.

- Thiede, R.C., Ehlers, T.A., Bookhagen, B. and Strecker, M.R. 2009. "Erosional variability along the northwest Himalaya". *Journal of Geophysical Research: Earth Surface* 114 F101015.
- Vannay, J.C., Grasemann, B., Rahn, M., Frank, W., Carter, A., Baudraz, V. and Cosca, M. 2004. "Miocene to Holocene exhumation of metamorphic crustal wedges in the NW Himalaya: Evidence for tectonic extrusion coupled to fluvial erosion". *Tectonics* 23 TC1014.
- Voellmy, A. 1955. "On the destructive force of avalanches", *Translation No. 2*. Avalanche Study Center, United States Department of Agriculture, USA.
- Wong, F.S. 1984. "Uncertainties in FE modelling of slope stability". *Computers & structures* 19(5-6): 777-791.
- Wulf, H., Bookhagen, B. and Scherler, D. 2012. "Climatic and geologic controls on suspended sediment flux in the Sutlej River Valley, western Himalaya". *Hydrology and Earth System Sciences* 16(7): 2193-2217.
- Yu, G., Zhang, M., Chen, H., 2014. "The dynamic process and sensitivity analysis for debris flow". In: *Sassa, K., Canuti, P., Yin, Y. (Eds.), Landslide Science for a Safer Geoenvironment*. Springer.
- Zhang, P. W. and Chen, Z. Y. 2006. "Influences of soil elastic modulus and Poisson's ratio on slope stability". *YantuLixue (Rock and Soil Mechanics)* 27(2): 299-303.
- Zienkiewicz, O. C., Humpheson, C. and Lewis, R. W. 1975. "Associated and non-associated viscoplasticity and plasticity in soil mechanics". *Geotechnique* 25(4): 671-689.

LIST OF FIGURES AND TABLES

Fig. 1 Geological setting. WGC: Wangtu Gneissic Complex. The red dashed circle in the inset represents the region within 100 km radius from the Satluj River (marked as blue line) that was used to determine the earthquake distribution in the area. KCF in inset refers to Kaurik-Chango Fault. The numbers 1-44 refer to serial number of landslides in Table 1.

Fig. 2 Field photographs of some of the landslides (a) Khokpa landslide (S.N.1); (b) Akpa_III landslide (S.N. 5); (c) Rarang landslide (S.N. 6); (d) Pawari landslide (S.N.14); (e) Urni landslide (S.N.19); (f) Barauni Gad_I_S landslide (S.N. 38). Black circle in the pictures that encircles the vehicle is intended to represent the relative scale.

Fig. 3 The FEM configuration of some of the slope models. S.N. refers to the serial no. of landslides in Table 1. The joint distribution in all the slopes was parallel-statistical with the normal distribution of joint spacing.

Fig. 4 The FEM analysis of all forty-four landslides. Grey bar in the background highlights the Higher Himalaya Crystalline (HHC) region that comprises relatively more unstable

landslides, relatively more landslide volume and human population. Source of human population: Census 2011 (Govt. of India, New Delhi). TS, KKG, HHC, LHC and LHS are Tethyan Sequence, Kinnaur Kailash Granite, Higher Himalaya Crystalline, Lesser Himalaya Crystalline and Lesser Himalaya Sequence, respectively

Fig. 5 Relationship of Factor of Safety (FS), Total Displacement (TD) and Shear Strain (SS). DS, RF, and RA refer to Debris slide, rock fall and rock avalanche, respectively.

Fig. 6 Parametric analysis of debris slides. (a) Akpa_III (S.N. 5); (b) Pangi_III (S.N. 13); (c) Barauni Gad_I_S (S.N. 38). S. N. refers to the serial no. of landslides in Table 1.

Fig. 7 Parametric analysis of rockfall/rock avalanche. (a) Tirung khad (S.N. 2); (b) Baren Dogri (S.No. 7); (c) Chagaon_II (S.N. 21).

Fig. 8 Landslide damming indices (a) Morphological Obstruction Index (MOI); (b) Hydro-morphological dam stability index (HDSI); (c) Landslides vs. MOI; (d) Landslides vs. HDSI.

Fig. 9 Potential landslide damming locations. (a) Akpa_III landslide; (b) Baren dogri landslide; (c) Pawari landslide; (d) Telangi landslide; (e) Urni landslide.

Fig. 10 Field signatures of the landslide damming near Akpa_III landslide. (a) Upstream view of Akpa landslide with lacustrine deposit at the left bank; (b) enlarged view of the lacustrine deposit with an arrow indicating the lacustrine sequence; (c) alternating fine-coarse sediments. F and C refer to fine (covered by yellow dashed lines) and coarse (covered by green dashed lines) sediments, respectively.

Fig. 11 Rainfall distribution. (a) Topographic profile; (b) annual rainfall; (c) monsoonal (June-Sep.) rainfall; (d) non-monsoonal (Oct.-May) rainfall. Green bars represent the years of relatively more rainfall resulting into the flash floods, landslides and socio-economic loss in the region. (i): hpenvs.nic.in, retrieved on March 1, 2020; Department of Revenue, Govt. of H.P. (ii): hpenvs.nic.in, retrieved on March 1, 2020. (iii): Kumar et al., 2019a; ndma.gov.in, retrieved on March 1, 2020 (iv): sandrp.in, retrieved on March 1, 2020. The numbers 1-44 refer to serial number of the landslides.

Fig. 12 Earthquake distribution. (a) Spatial variation of earthquakes. The transparent circle represents the region within 100 km radius from the Satluj River (blue line). The black

dashed line represents the seismic dominance around the Kaurik-Chango fault;(b) earthquake magnitude vs. focal depth. The red dashed region highlights the concentration of earthquakes within 40 km depth; (c) Cross section view (Based on Hazarika et al. 2017; Bilham 2019). Red dashed circle represents the zone of strain accumulation caused by the Indian and Eurasian plate collision (Bilham 2019). ISC: International Seismological Centre. SD, MCT, MT, MBT and HFT are Sangla Detachment, Main Central Thrust, Munsiri Thrust, Main Boundary Thrust and Himalayan Frontal Thrust, respectively.

Fig. 13 Results of the run-out analysis. μ refers to coefficient of friction.

Fig. 14 Results of run-out analysis at different values of μ and ξ . μ and ξ refer to coefficient of friction and turbulence, respectively.

Table 1 Details of the landslides used in the study.

Table 2 Details of the satellite imagery.

Table 3 Criteria used in the Finite Element Method (FEM) analysis.

Table 4 Details of input parameters used in the run-out analysis.

S.N.	Landslide location	Latitude/ Longitude	Type	Area ¹ , m ²	Volume ² , m ³	Human population ³	Litho- tectonic division
1	Khokpa	31°35'18.9"N 78°26'28.6"E	Debris slide	21897± 241	43794± 18361	373	Tethyan Sequence (TS)
2	Tirung Khad	31°34'50.4"N 78°26'20.5"E	Rockfall	28537± 314	14269± 9055	0	
3	Akpa_I	31°34'57.1"N 78°24'30.6"E	Rock avalanche	963051± 10594	1926102± 807515	0	TS-KKG
4	Akpa_II	31°35'2.2"N 78°23'25.4"E	Rock avalanche	95902± 1055	143853± 40734	470	Kinnaur Kailash Granite (KKG)
5	Akpa_III	31°34'54.5"N 78°23'2.4"E	Debris slide	379570± 4175	7591400± 3182681	1617	
6	Rarang	31°35'58.7"N 78°20'39.1"E	Rockfall	4586± 50	4586± 1923	848	Higher Himalaya Crystalline (HHC)
7	Baren Dogri	31°36'23.6"N 78°20'23.1"E	Rock avalanche	483721± 5321	2418605±421561	142	
8	Thopan Dogri	31°36'12.3"N 78°19'50.4"E	Rockfall	55296± 608	165888± 46974	103	
9	Kashang Khad_I	31°36'5.0"N 78°18'44.4"E	Debris slide	113054± 1244	169581± 48019	103	
10	Kashang Khad_II	31°35'58.3"N 78°18'34.0"E	Rockfall	27171± 299	40757± 11541	103	
11	Pangi_I	31°35'36.4"N 78°17'36.4"E	Debris slide	30112± 331	45168± 12790	1389	
12	Pangi_II	31°35'38.9"N 78°17'12.2"E	Debris slide	59436± 654	118872± 49837	1389	
13	Pangi_III	31°34'38.9"N 78°16'55.6"E	Debris slide	75396± 829	188490± 32854	7	
14	Pawari	31°33'49.8"N 78°16'28.6"E	Debris slide	320564± 3526	1602820± 279370	4427	
15	Telang	31°33'7.0"N 78°16'37.2"E	Debris slide	543343± 5977	13583575± 2367608	6817	
16	Shongthong	31°31'13.0"N 78°16'17.0"E	Debris slide	5727± 63	11454± 2464	388	Lesser Himalaya Crystalline (LHC)
17	Karchham	31°30'12.4"N 78°11'30.8"E	Rock avalanche	28046± 309	56092± 23516	0	
18	Choling	31°31'17.0"N 78° 8'4.9"E	Debris slide	20977± 231	20977± 8795	0	
19	Urni	31°31'8.0"N 78° 7'42.2"E	Debris slide	112097± 1233	1120970± 469965	500	
20	Chagaon_I	31°30'55.9"N 78° 6'52.0"E	Rockfall	3220± 35	3220± 1350	0	
21	Chagaon_II	31°30'57.9"N 78° 6'47.7"E	Rockfall	11652± 128	11652± 4885	0	

22	Chagaon_III	31°31'3.0"N 78° 6'21.4"E	Debris slide	42141± 464	168564± 70670	1085	
23	Wangtu_U/s	31°32'4.8"N 78° 3'5.0"E	Rock avalanche	211599± 2328	317399± 89876	17	
24	Wangtu D/s__1	31°33'27.7"N 77°59'43.7"E	Debris slide	4655± 51	9310± 3903	71	
25	Kandar	31°33'43.7"N 77°59'54.9"E	Rock avalanche	151128± 1662	302256± 126720	186	
26	Wangtu D/s_2	31°33'38.9"N 77°59'29.9"E	Debris slide	8004± 88	16008± 6711	71	
27	Agade	31°33'52.3"N 77°58'3.5"E	Debris slide	9767± 107	14651± 4149	356	
28	Punaspa	31°33'37.6"N 77°57'31.5"E	Debris slide	3211± 35	3211± 1346	343	
29	Sungra	31°33'58.8"N 77°56'49.6"E	Debris slide	5560± 61	11120± 4662	2669	
30	Chota Kamba	31°33'39.2"N 77°54'39.0"E	Rock avalanche	197290± 2170	591870± 167597	401	
31	Bara Kamba	31°34'10.4"N 77°52'56.7"E	Rockfall	36347± 400	18174± 7619	564	
32	Karape	31°33'44.9"N 77°53'13.9"E	Debris slide	50979± 561	50979± 21373	1118	
33	Pashpa	31°34'40.2"N 77°50'53.0"E	Rockfall	16079± 171	8040± 3371	29	
34	Khani Dhar_I	31°33'43.4"N 77°48'52.5"E	Rock avalanche	218688± 2406	874752± 366738	0	
35	Khani Dhar_II	31°33'26.3"N 77°48'35.8"E	Rock avalanche	146994± 1617	734970± 248125	0	
36	Khani Dhar_III	31°33'20.1"N 77°48'27.8"E	Rock avalanche	20902± 230	62706± 17756	0	
37	Jeori	31°31'58.8"N 77°46'18.2"E	Rock avalanche	93705± 1031	93705± 39286	0	
38	Barauni Gad_I_S	31°28'56.6"N 77°41'40.4"E	Debris slide	63241± 696	758892± 111620	236	LHC-LHS
39	Barauni Gad_I_Q	31°29'00.0"N 77°41'38.0"E	Debris slide	59273± 652	711276± 104616	0	Lesser Himalaya Sequence (LHS)
40	Barauni Gad_II	31°28'43.9"N 77°41'24.6"E	Rockfall	6977± 77	3489± 1463	0	
41	Barauni Gad_III	31°29'5.6"N 77°41'23.7"E	Rockfall	33115± 364	33115± 13883	0	
42	D/s Barauni Gad_I	31°28'24.9"N 77°41'8.4"E	Rockfall	19101± 210	19101± 8008	0	
43	D/s Barauni Gad_II	31°28'25.5"N 77°40'56.7"E	Rockfall	21236± 234	21236± 8903	0	
44	D/s Barauni Gad_III	31°28'7.4"N 77°40'42.4"E	Rockfall	15632± 172	15632± 6554	0	

¹Error (\pm) caused by GE measurement (1.06 %).

²Error (\pm) is an outcome of multiplication of area \pm error and thickness \pm error. Thickness error (Std. dev.) corresponds to averaging of field based approximated thickness.

³The human population is based on census 2011, Govt. of India. The villages/town in the radius of 500 m from the landslide are considered to count the human population.

Table 1 Details of landslides used in the study.

Satellite data		Source	Date of data	Spatial resolution
CARTOSAT-1 stereo imagery	524/253	National Remote Sensing Center (NRSC), Hyderabad, India	5 th Dec. 2010	~2.5 m
	525/253		16 th Dec. 2010	~2.5 m
	526/252		18 th Oct. 2011	~2.5 m
	526/253		18 th Oct. 2011	~2.5 m
	527/252		24 th Nov. 2010	~2.5 m
	527/253		27 th Dec. 2010	~2.5 m
	528/252		26 th Nov. 2011	~2.5 m

Table 2 Details of satellite imagery.

Table 3 Criteria used in the Finite Element Method (FEM) analysis.

	Material Criteria	Parameters	Source
Rockmass	<p>Generalized Hoek & Brown (GHB) Criteria (Hoek et al. 1995)</p> $\sigma_1 = \sigma_3 + \sigma_{ci} [m_b (\sigma_3 / \sigma_{ci}) + s]^a$ <p>Here, σ_1 and σ_3 are major and minor effective principal stresses at failure; σ_{ci}, compressive strength of intact rock; m_b, a reduced value of the material constant (m_i) and is given by;</p> $m_b = m_i e^{[(GSI-100)/(28-14D]}$ <p>s and a; constants for the rock mass given by the following relationships;</p> $s = e^{[(GSI-100)/(9-3D]}$ $a = \frac{1}{2} + \frac{1}{6} \left[e^{\left[-\left(\frac{GSI}{15}\right)\right]} - e^{\left[-\left(\frac{20}{3}\right)\right]} \right]$ <p>Here, D; a factor which depends upon the degree of disturbance to which the rock mass has been subjected by blast damage and stress relaxation. GSI (Geological Strength Index); a rockmass characterization parameter.</p>	Unit Weight, γ (MN/m ³)	Laboratory analysis (UCS) (IS: 9143-1979)
		Uniaxial Compressive Strength, σ_{ci} (MPa)	
		Rockmass modulus (MPa)	Laboratory analysis (Ultrasonic velocity test); Hoek and Diederichs (2006).
		Poisson's Ratio	
		Geological Strength Index	Field observation and based on recent amendments (Cai et al. 2007 and reference therein)
		Material Constant (m_i)	Standard values (Hoek and Brown 1997)
		m_b	GSI was field dependedent, m_i as per(Hoek and Brown 1997) and D is used between 0-1 in view of rockmass exposure and blasting.
		s	
		a	
		D	
Joint	<p>Barton-Bandis Criteria (Barton and Choubey 1977; Barton and Bandis 1990)</p> $\tau = \sigma_n \tan [\phi_r + JRC \log_{10} (JCS / \sigma_n)]$ <p>Here, τ is joint shear strength; σ_n, normal stress across joint; ϕ_r, reduced friction angle; JRC, joint roughness coefficient; JCS, joint compressive strength.</p> <p>JRC is based on the chart of Barton and Choubey (1977); Jang et al. (2014). JCS was determined using following equation;</p> $\log_{10}(JCS) = 0.00088 (R_L)(\gamma) + 1.01$ <p>Here, R_L isSchimdt Hammer Rebound value and γ is unit weight of rock.</p> <p>The JRC and JCS were used as JRC_n and JCS_n following the scale corrections observed by Barton and Choubey</p>	Normal Stiffness, k_n (MPa/m)	E_i is lab dependent. L and GSI were field dependedent. D is used between 0-1 in view of rockmass exposure and blasting.
		Shear Stiffness, k_s (MPa/m)	It is assumed as $k_n/10$. However, effect of denominator is aslo obtainedthrough parameteric study.
		Reduced friction angle, ϕ_r	Standard values (Barton and Choubey 1977).
		Joint roughness coefficient, JRC	Field based data from profilometer and standard values from Barton and Choubey (1977); Jang et al. (2014).

	<p>(1977) and reference therein and proposed by Barton and Bandis (1982).</p> $JRC_n = [JRC(L/L_o)^{-0.02(JRC)}]$ $JCS_n = [JCS(L/L_o)^{-0.03(JRC)}]$ <p>Here, L and L_o are mean joint spacing in field and, respectively. L_o has been suggested to be 10 cm.</p> <p>Joint stiffness criteria (Barton 1972)</p> $k_n = (E_i * E_m) / L * (E_i - E_m)$ <p>Here, k_n; Normal stiffness, E_i; Intact rock modulus, E_m; Rockmass modulus L; Mean joint spacing.</p> $E_m = (E_i) * [0.02 + \{1 - D/2\} / \{1 + e^{(60 + 15 * D - GSI)/11}\}]$ <p>Here, E_m is based on Hoek and Diederichs (2006) and reference therein</p>	Joint compressive strength, JCS (MPa)	Empirical equation of Deere and Miller (1966) relating Schmidt Hammer Rebound (SHR) values, σ_{ci} and unit weight of rock. SHR was field dependent.
		Scale corrected, JRC_n	Empirical equation of Barton and Bandis (1982).
		Scale corrected, JCS_n (MPa)	
Soil	<p>Mohr-Coulomb Criteria (Coulomb 1776; Mohr 1914)</p> $\tau = C + \sigma \tan \phi$ <p>Here, τ; Shear stress at failure, C; Cohesion, σ_n; normal strength, ϕ; angle of friction.</p>	Unit Weight (MN/m ³)	Laboratory analysis (UCS) (IS: 2720-Part 4-1985; IS: 2720-Part 10-1991)
		Young's Modulus, E_i (MPa)	Laboratory analysis (UCS); IS: 2720-Part 10-1991.
		Poisson's Ratio	Standard values from Bowles (1996)
		Cohesion, C (MPa)	Laboratory analysis (Direct shear) (IS: 2720-Part 13- 1986)
		Friction angle, ϕ	

Landslide	Material type	Material depth¹, m	Friction coefficient²	Turbulence coefficient³, m/sec²
Akpa (S.N. 5)	Gravelly sand	5	$\mu = 0.05, 0.1, 0.3$	$\xi = 100, 200, 300$
Baren Dogri (S.N. 7)	Gravelly sand	1.25	$\mu = 0.05, 0.1, 0.4$	$\xi = 100, 200, 300$
Pawari (S.N. 14)	Gravelly sand	1.25	$\mu = 0.05, 0.1, 0.4$	$\xi = 100, 200, 300$
Telangi (S.N. 15)	Gravelly sand	6.25	$\mu = 0.05, 0.1, 0.4$	$\xi = 100, 200, 300$
Urni (S.N. 19)	Gravelly sand	2.5	$\mu = 0.06, 0.1, 0.4$	$\xi = 100, 200, 300$

¹ Considering that fact that during slope failure, irrespective of type of trigger, entire loose material might not slide down, the depth is taken as only $\frac{1}{4}$ (thickness) in the calculation.² Since the angle of run-out track (slope and river channel) varied a little beyond the suggested range 2.8° - 21.8° or $\mu = 0.05$ - 0.4 (Hung et al., 1984; RAMMS v.1.7.0), we kept out input in this suggested range wherever possible to avoid simulation uncertainty. ³This range is used in view of the type of loose material i.e., granular in this study (RAMMS v.1.7.0).

Table 4 Details of input parameters for run-out analysis. S.N. refers to serial number of landslides in Fig. 1.

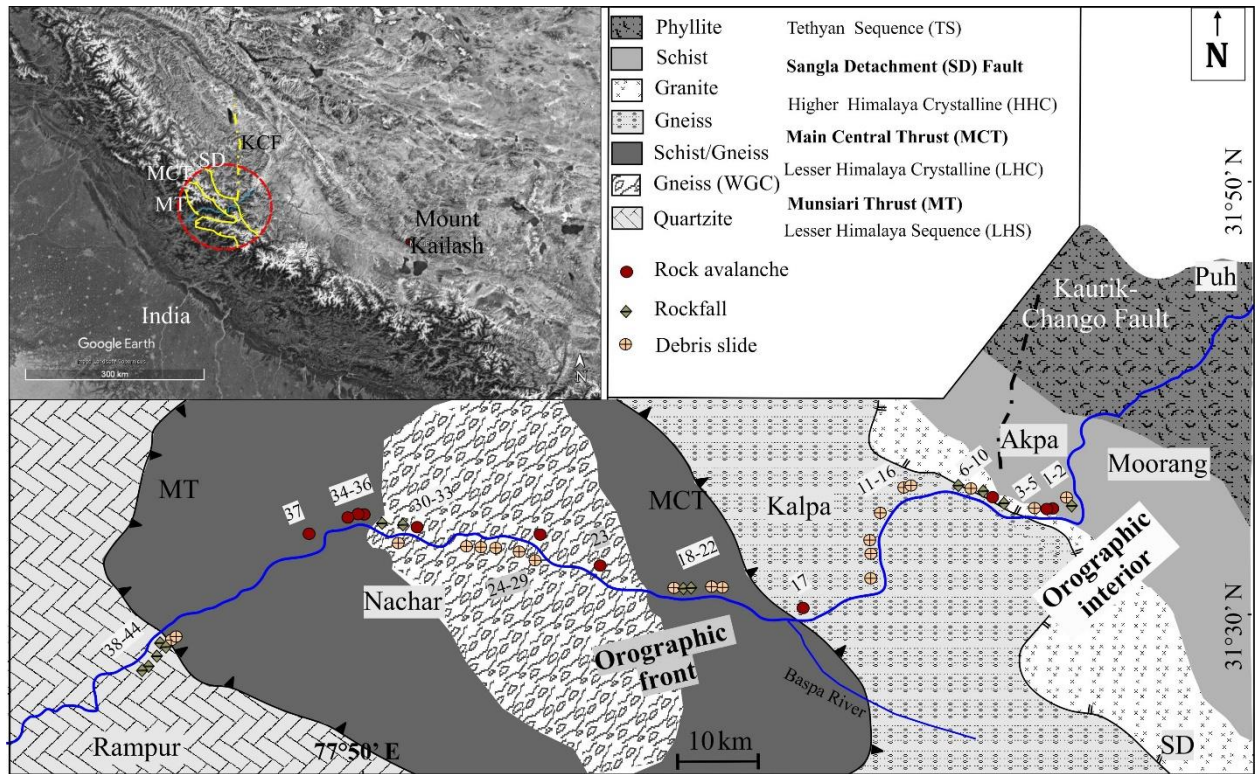


Fig. 1 Geological setting. WGC: Wangtu Gneissic Complex. The red dashed circle in the inset represents the region within 100 km radius from the Satluj River (marked as blue line) that was used to determine the earthquake distribution in the area. KCF in inset refers to Kaurik-Chango Fault. The numbers 1-44 refer to serial number of landslides in Table 1.

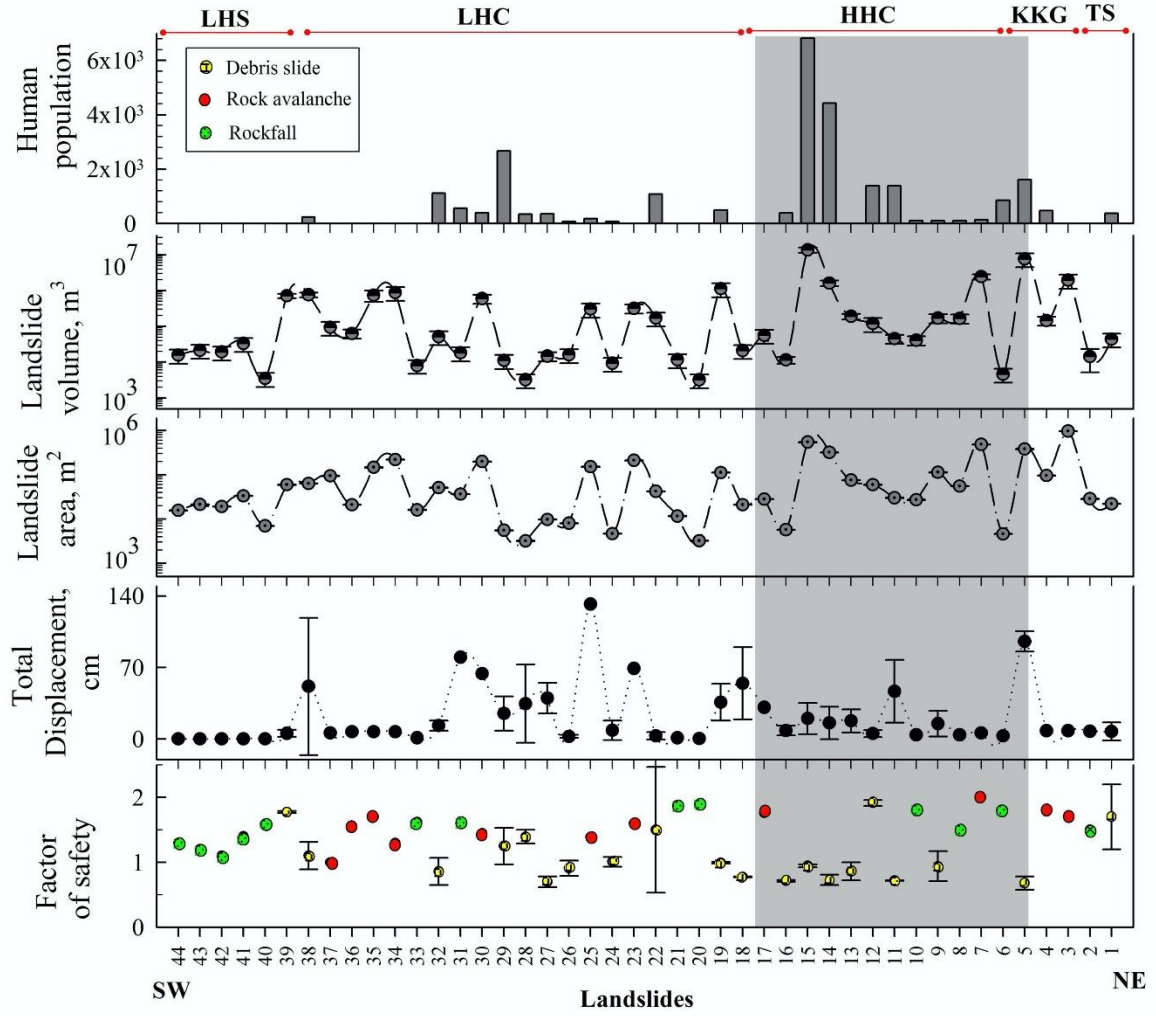


Fig. 4 The FEM analysis of all forty-four landslides. Grey bar in the background highlights the Higher Himalaya Crystalline (HHC) region that comprises relatively more unstable landslides, relatively more landslide volume and human population. Source of human population: Census 2011 (Govt. of India, New Delhi). TS, KKG, HHC, LHC and LHS are Tethyan Sequence, Kinnaur Kailash Granite, Higher Himalaya Crystalline, Lesser Himalaya Crystalline and Lesser Himalaya Sequence, respectively

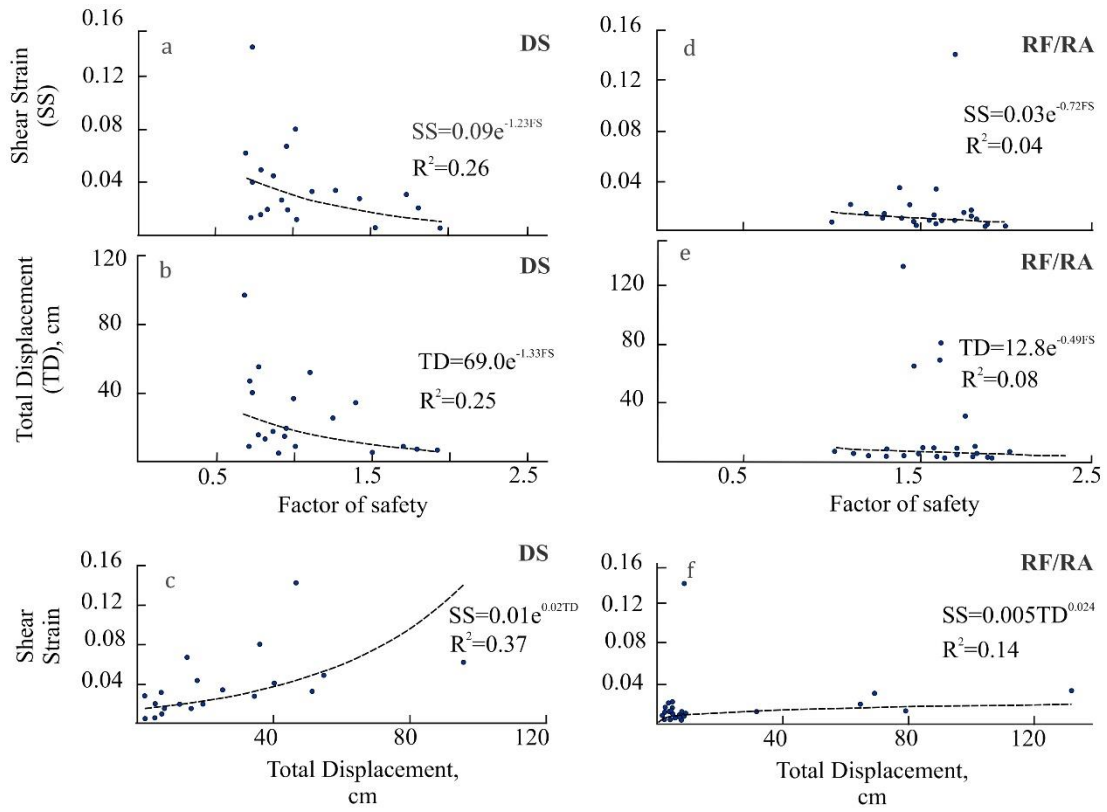


Fig. 5 Relationship of Factor of Safety (FS), Total Displacement (TD) and Shear Strain (SS).
DS, RF, and RA refer to Debris slide, rock fall and rock avalanche, respectively.

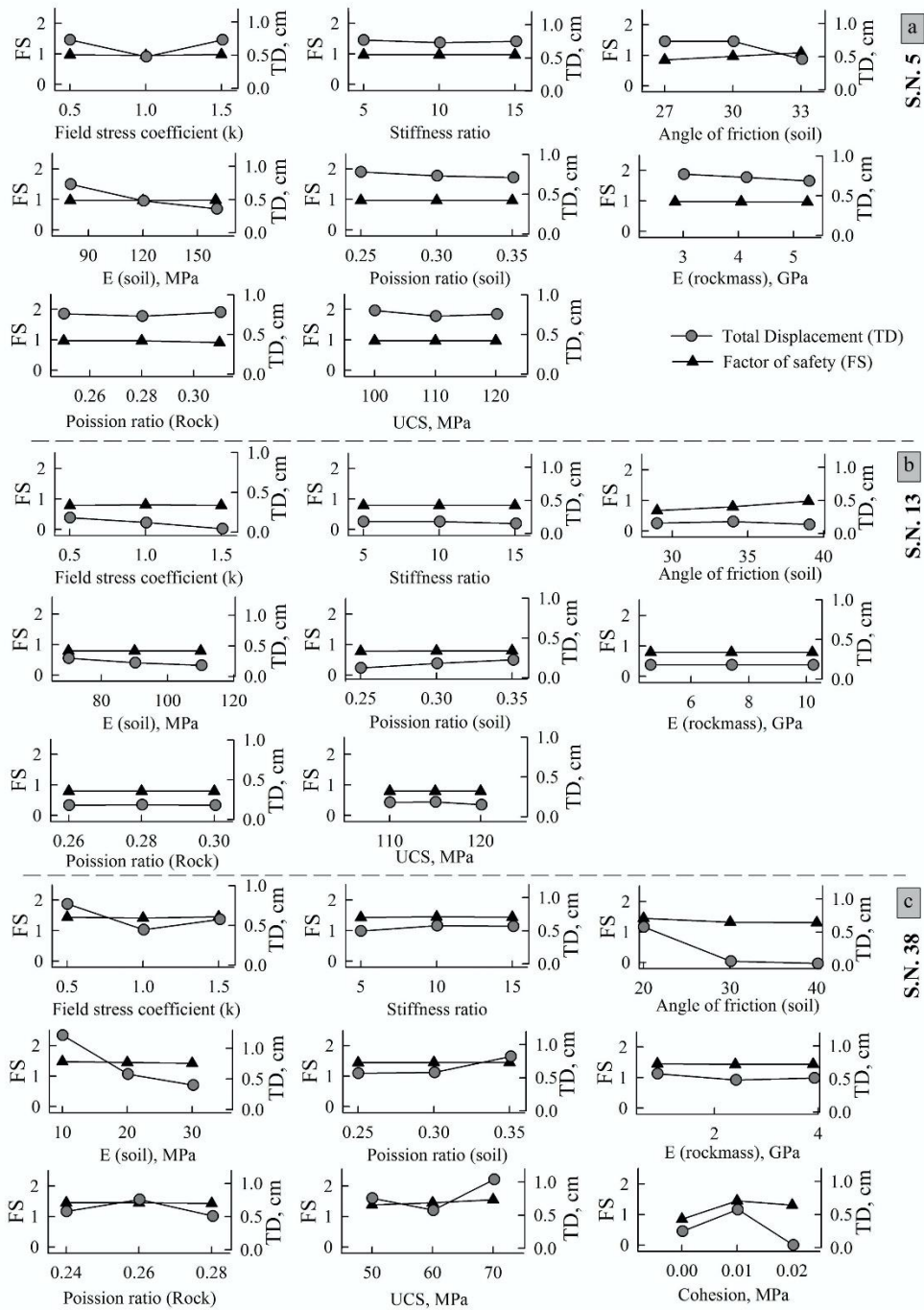


Fig. 6 Parametric analysis of debris slides. (a) Akpa_III (S.N. 5); (b) Pangi_III (S.N. 13); (c) Barauni Gad_I_S (S.N. 38). S. N. refers to the serial no. of landslides in Table 1.

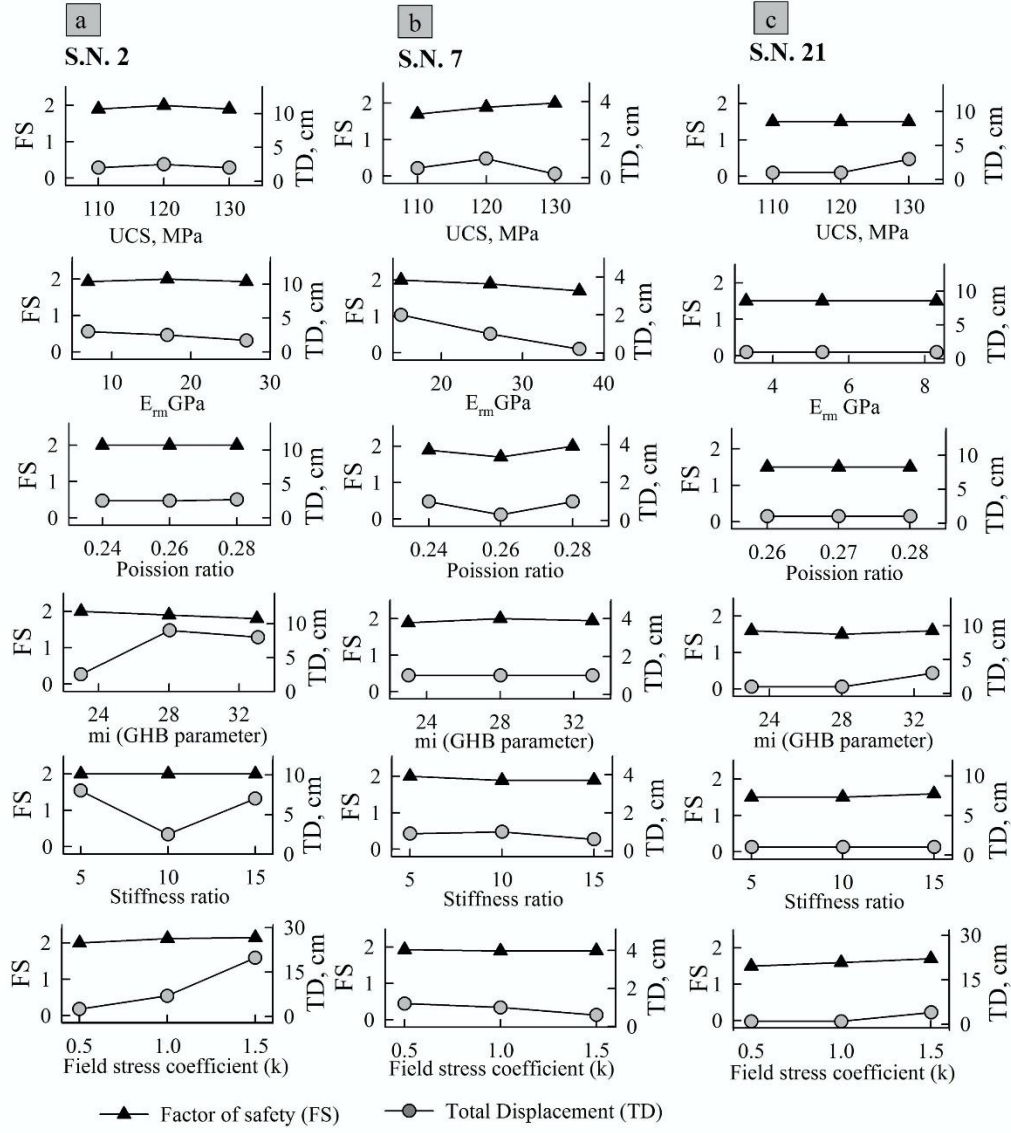


Fig. 7 Parametric analysis of rockfall/rock avalanche. (a) Tirung khad (S.N. 2); (b) Baren Dogri (S.No. 7); (c) Chagaon_II (S.N. 21).

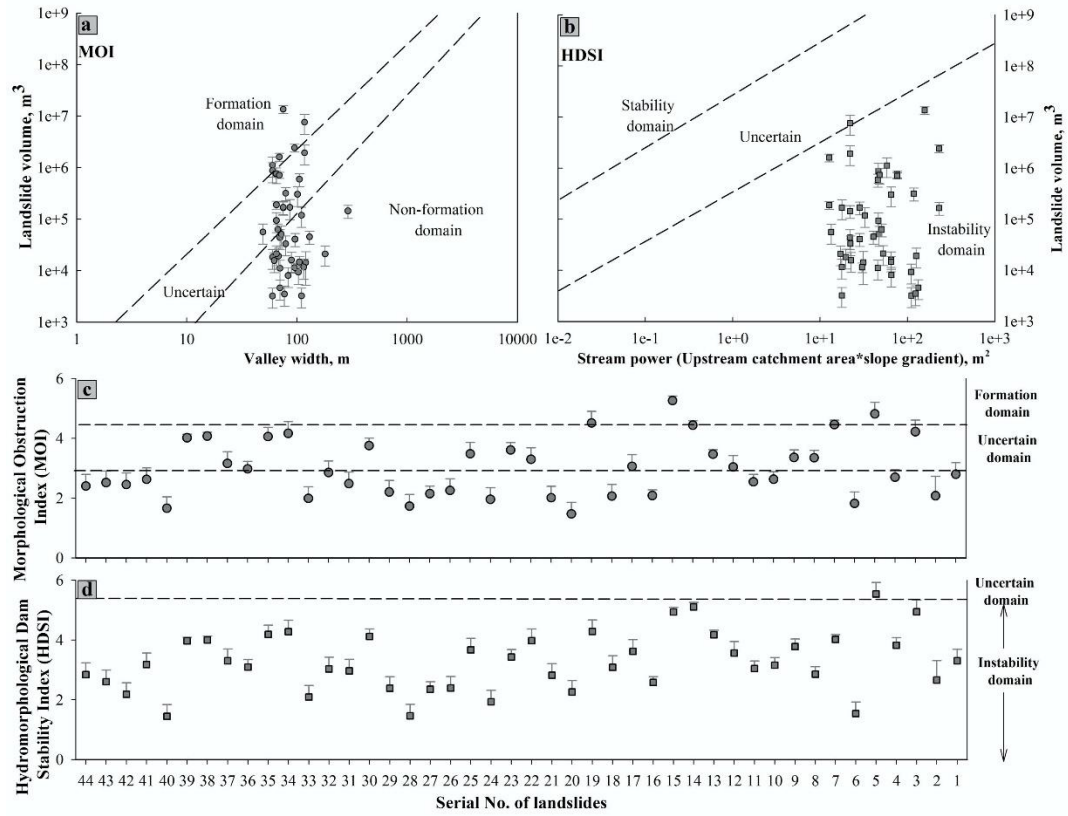


Fig. 8 Landslide damming indices (a) Morphological Obstruction Index (MOI); (b) Hydro-morphological dam stability index (HDSI); (c) Landslides vs. MOI; (d) Landslides vs. HDSI.

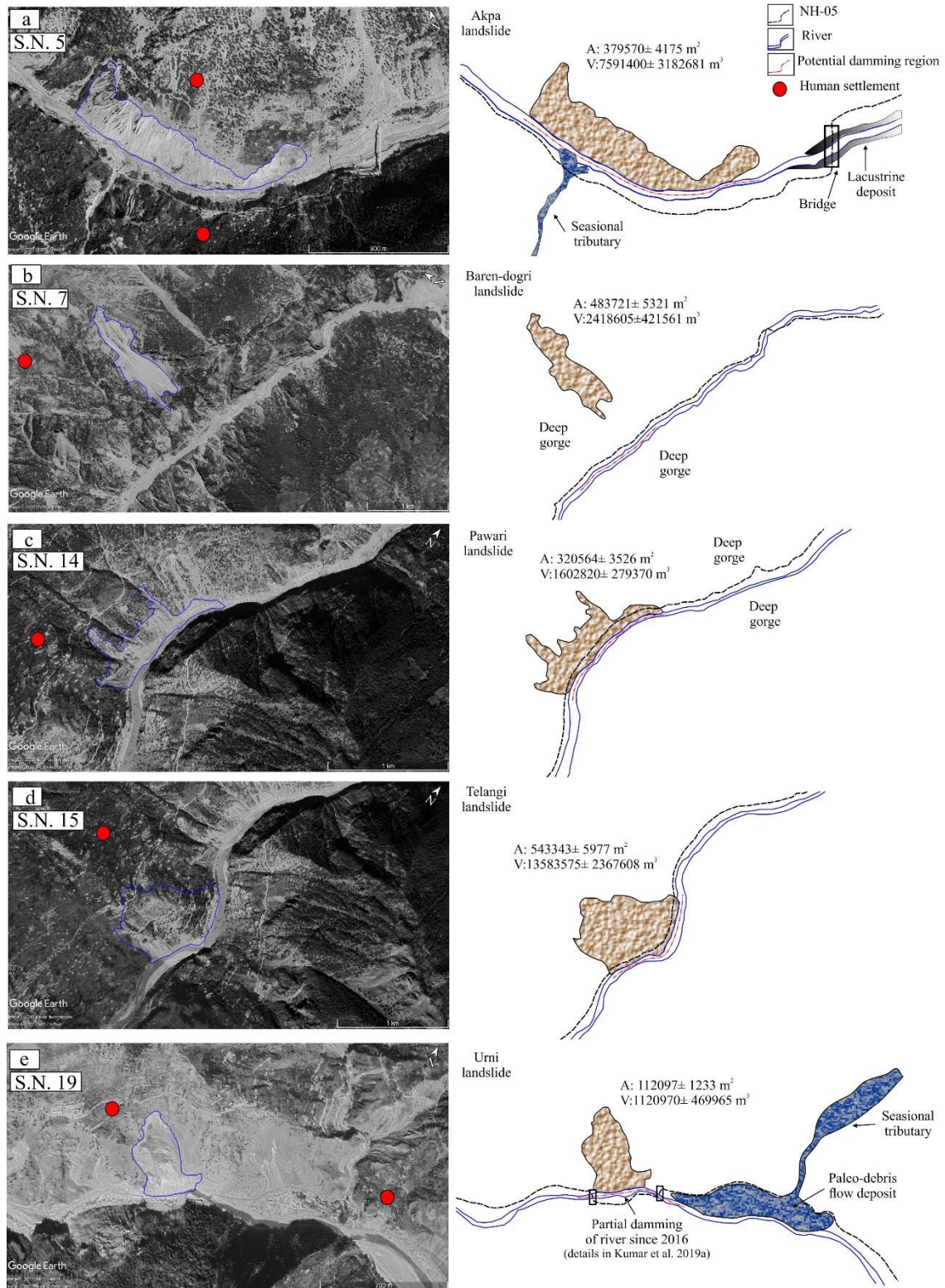


Fig. 9 Potential landslide damming locations. (a) Akpa_III landslide; (b) Baren dogri landslide; (c) Pawari landslide; (d) Telangi landslide; (e) Urni landslide.

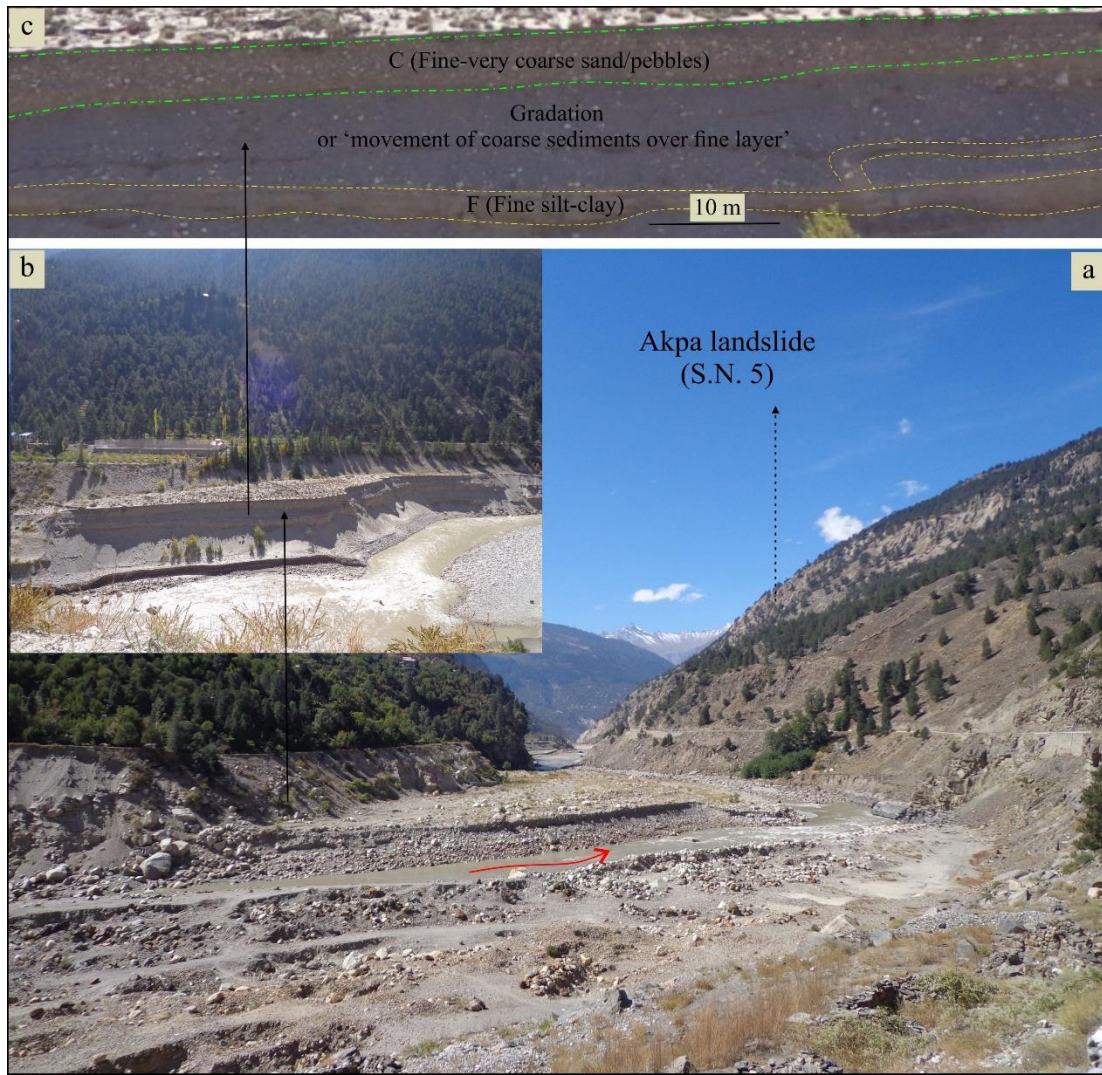


Fig. 10 Field signatures of the landslide damming near Akpa_III landslide. (a) Upstream view of Akpa landslide with lacustrine deposit at the left bank; (b) enlarged view of the lacustrine deposit with an arrow indicating the lacustrine sequence; (c) alternating fine-coarse sediments. F and C refer to fine (covered by yellow dashed lines) and coarse (covered by green dashed lines) sediments, respectively.

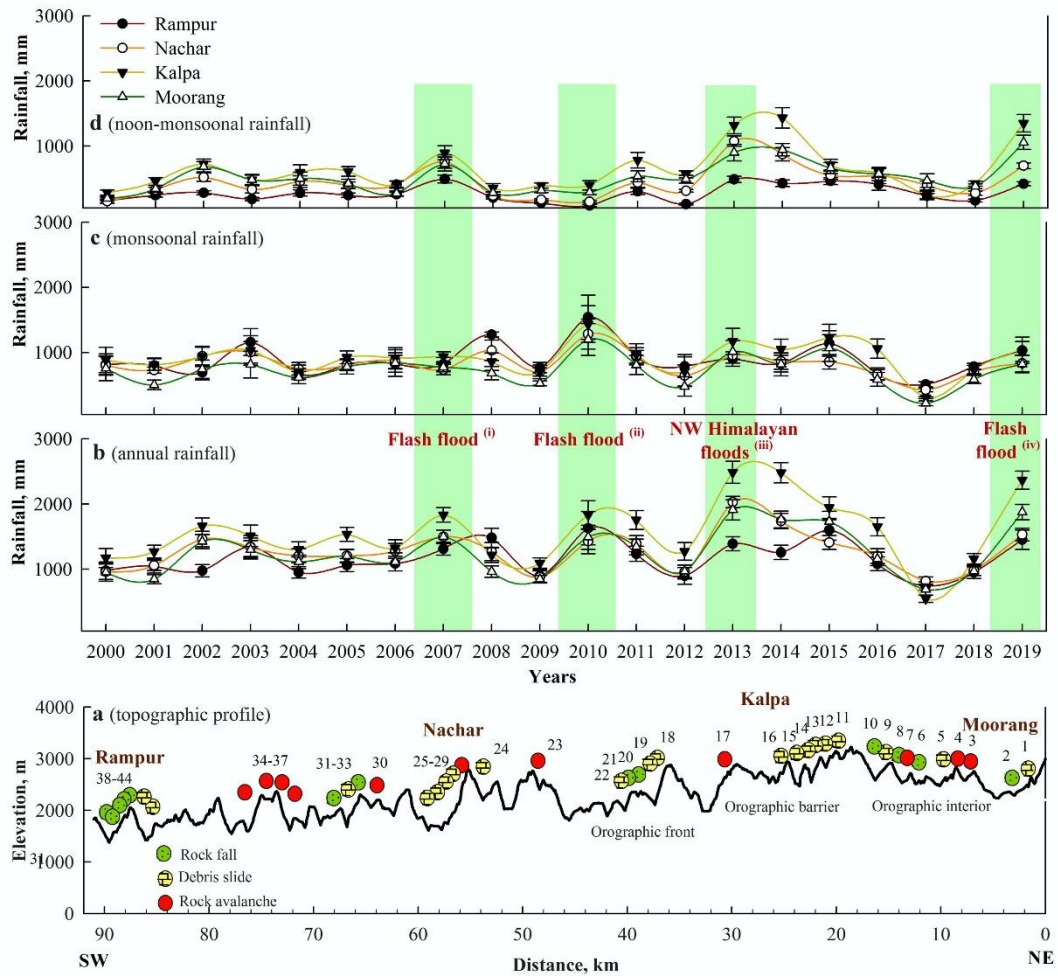


Fig. 11 Rainfall distribution. (a) Topographic profile; (b) annual rainfall; (c) monsoonal (June-Sep.) rainfall; (d) non-monsoonal (Oct.-May) rainfall. Green bars represent the years of relatively more rainfall resulting into the flash floods, landslides and socio-economic loss in the region. (i):hpenvis.nic.in, retrieved on March 1, 2020; Department of Revenue, Govt. of H.P. (ii): hpenvis.nic.in, retrieved on March 1, 2020.(iii): Kumar et al., 2019a;ndma.gov.in, retrieved on march 1, 2020 (iv):sandrp.in, retrieved on march 1, 2020.The numbers 1-44 refer to serial number of the landslides.

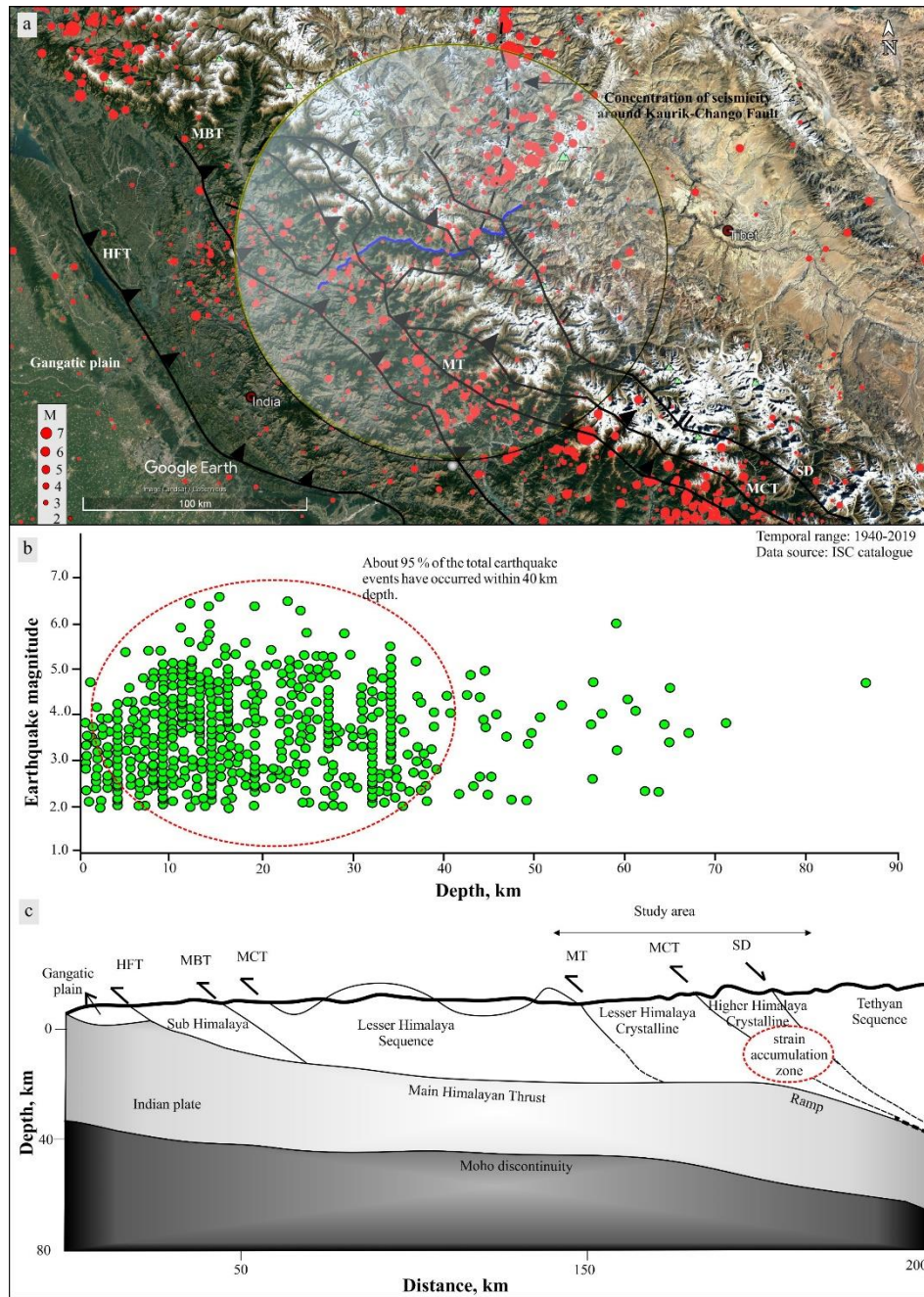


Fig. 12 Earthquake distribution. (a) Spatial variation of earthquakes. The transparent circle represents the region within 100 km radius from the Satluj River (blue line). The black dashed line represents the seismic dominance around the Kaurik-Chango fault; (b) earthquake magnitude vs. focal depth. The red dashed region highlights the concentration of earthquakes within 40 km depth; (c) Cross section view (Based on Hazarika et al. 2017; Bilham, 2019). Red dashed circle represents the zone of strain accumulation caused by the Indian and Eurasian plate collision (Bilham, 2019). ISC: International Seismological Centre. HFT: Himalayan Frontal Thrust.

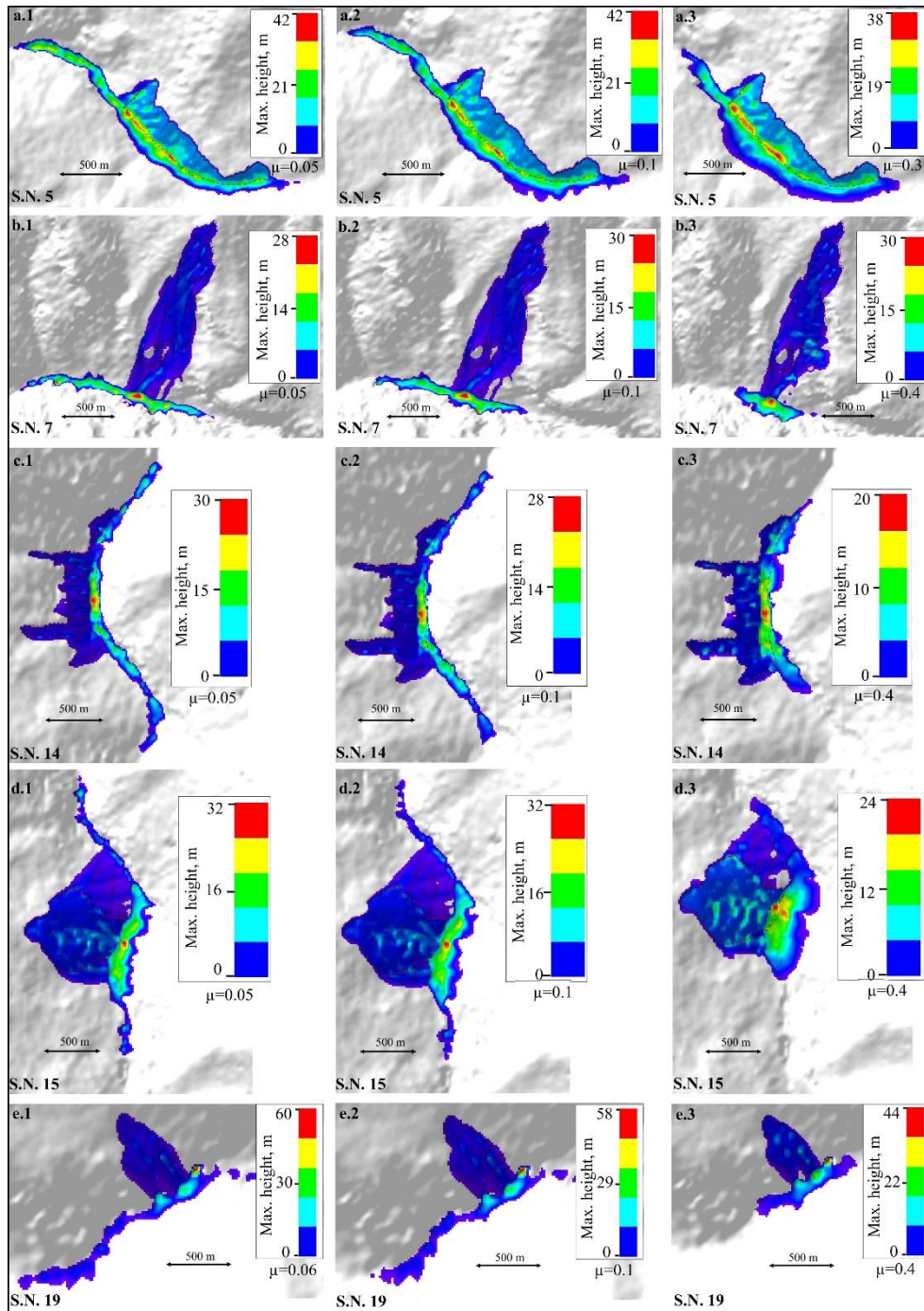


Fig. 13 Results of the run-out analysis. μ refers to coefficient of friction.

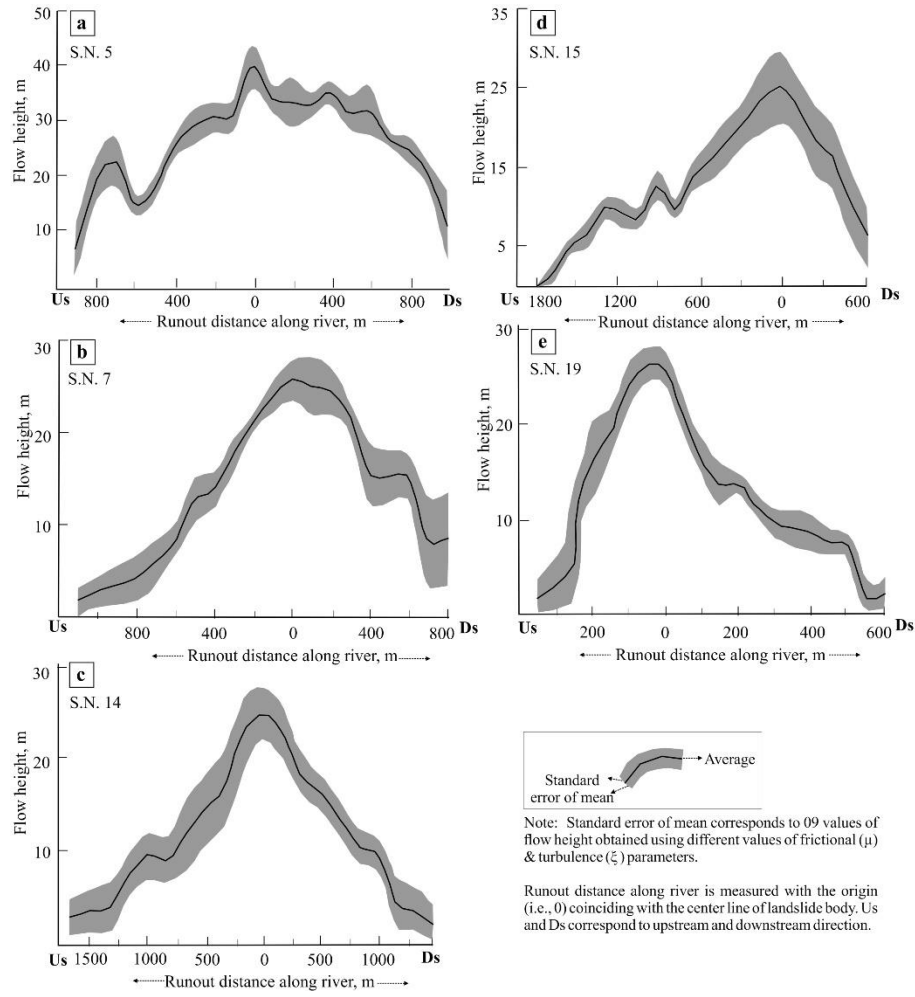


Fig. 14 Results of run-out analysis at different values of μ and ξ . μ and ξ refer to coefficient of friction and turbulence, respectively.